Molecular Cell

Article

Metabolic profiling reveals pyrimidine synthesis enzyme CAD as a central carbon metabolism signaling node in cancer cell proliferation

Graphical abstract

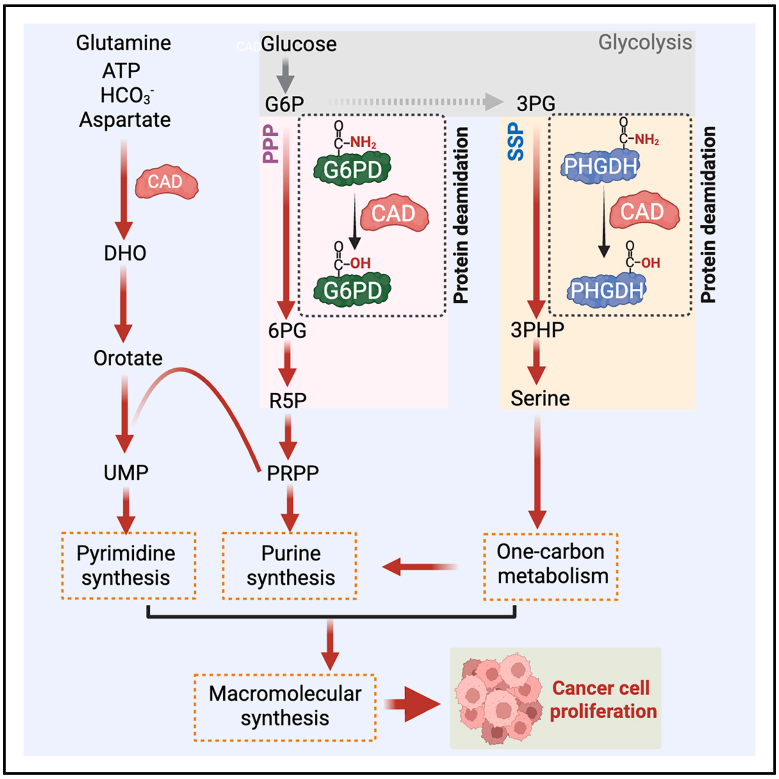

Highlights

- CAD fuels cancer cell proliferation that requires more than pyrimidine synthesis
- CAD deamidates and activates G6PD and PHGDH to rewire carbon metabolism
- The glutaminase domain of CAD rewires carbon metabolism via deamidation
- A signature of metabolic rewiring activated by CAD underpins human HCC

Authors

Chao Qin, Zhenhao An, Shu Feng, ..., Charles Brenner, Takeshi Saito, Pinghui Feng

Correspondence

pinghuif@usc.edu

In brief

Qin et al. show that the pyrimidine synthesis enzyme CAD reprograms central carbon metabolism by deamidating G6PD and PHGDH, thereby fueling the formation of tumors, including hepatocarcinoma. Targeting the unconventional enzyme activity of CAD offers a promising therapeutic strategy.

Qin et al., 2026, Molecular Cell *86*, 1529–1545
April 16, 2026
https://doi.org/10.1016/j.molcel.2026.03.016

CellPress

Molecular Cell

CellPress

Article

Metabolic profiling reveals pyrimidine synthesis enzyme CAD as a central carbon metabolism signaling node in cancer cell proliferation

Chao Qin,[1] Zhenhao An,[1] Shu Feng,[2,6] Wen Fu,[1] Xinchi Xie,[1] Ali Can Savas,[1] Taolin Xie,[1] Charles Brenner,[2] Takeshi Saito,[3,4,5] and Pinghui Feng[1,5,7,8,*]

[1]Section of Infection and Immunity, Herman Ostrow School of Dentistry, University of Southern California, Los Angeles, CA 90089, USA
[2]Department of Diabetes and Cancer Metabolism, Beckman Research Institute, City of Hope National Medical Center, Duarte, CA 91010, USA
[3]Division of Gastrointestinal and Liver Diseases, Department of Medicine, University of Southern California, Keck School of Medicine, Los Angeles, CA 90033, USA
[4]Department of Pathology, University of Southern California, Los Angeles, CA 90033, USA
[5]Department of Molecular Microbiology and Immunology, Norris Comprehensive Cancer Center, University of Southern California, Los Angeles, CA 90033, USA
[6]Department of Microbial Health Sciences and Center for Global Pathogen Infection, Cleveland Clinic Research, Cleveland, OH, USA
[7]Department of Microbial Health Sciences and Center for Global Pathogen Infection, Center for Experimental Therapeutics, Cleveland, OH, USA
[8]Lead contact
*Correspondence: pinghuif@usc.edu

https://doi.org/10.1016/j.molcel.2026.03.016

SUMMARY

Rapid cancer cell proliferation requires extensive macromolecular biosynthesis, yet how distinct anabolic pathways are coordinated remains incompletely understood. Here, we report that the trifunctional carbamoyl-phosphate synthase, aspartate transcarbamoylase, and dihydroorotase (CAD) activates key glycolytic enzymes to support biosynthesis and cancer cell proliferation. When cancer proteomics datasets were queried, a CAD activation signature was identified in diverse tumors. Metabolomics analysis revealed that CAD fuels central carbon metabolism, specifically the pentose phosphate pathway (PPP) and serine synthesis pathway (SSP). Mechanistically, CAD deamidates and activates glucose-6-phosphate dehydrogenase (G6PD) and phosphoglycerate dehydrogenase (PHGDH), rate-limiting enzymes of the PPP and SSP, respectively, which are fully recapitulated by the glutaminase domain of CAD. Functional interrogation of cancer-associated CAD mutations and human hepatocellular carcinoma tumors predicts the metabolic signature endowed by G6PD and PHGDH deamidation. Simultaneous inhibition of G6PD and PHGDH effectively impeded tumor formation. This work identifies CAD as a central carbon metabolism signaling node and a potential therapeutic target.

INTRODUCTION

Understanding cancer cell proliferation is imperative to develop antitumor therapy that targets cancer intrinsic mechanisms.[1,2] In preparation for division, cells double their biomass chiefly by synthesizing macromolecules.[3–5] Central to the metabolic program is the synthesis of the nucleotide that performs diverse functions in cell proliferation.[6,7] Glycolysis and its branch pathways, specifically the pentose phosphate pathway (PPP) and the serine synthesis pathway (SSP), provide the carbon source for *de novo* nucleotide synthesis, whereas glutaminolysis contributes both nitrogen and carbon to nucleobases.[8–10] How *de novo* nucleotide synthesis is coordinated with other carbon and nitrogen anabolic pathways is not fully understood.

CAD is a trifunctional enzyme that catalyzes the first three reactions of *de novo* pyrimidine synthesis.[11,12] It integrates diverse physiological stimuli to regulate pyrimidine synthesis, underpinning cell proliferation.[13–16] Extracellular stimuli, such as growth factors activate CAD via mechanistic target of rapamycin complex 1 (mTORC1) and ribosomal protein S6 kinase (S6K), the latter of which directly phosphorylates CAD at serine 1859, while substrates and pyrimidine products of CAD positively or negatively alter the allosteric oligomerization and the enzymatic activity of CAD.[12–14,17,18] How CAD-mediated pyrimidine synthesis communicates with other anabolic pathways to coordinate macromolecular synthesis during cell proliferation remains unknown.

CAD belongs to the glutamine amidotransferase (GAT) family.[19] These enzymes consist of multiple domains that catalyze several sequential reactions that share an amidotransfer reaction using glutamine.[20] Interestingly, some of these enzymes have been shown to catalyze the hydrolysis of asparaginyl and glutaminyl residues, converting them into their negatively charged counterpart, a process known as deamidation. Deamidation can dramatically alter the function of a target protein, implying its biological significance in health and disease.[21–29] Although metabolic enzymes are defined as executors that metabolize small-molecule intermediates, their roles beyond metabolism are rudimentary at best. Here, we report that CAD deamidates and activates G6PD and PHGDH, the rate-limiting enzymes of the PPP and SSP, respectively. Notably, the glutaminase domain of CAD is sufficient to catalyze the deamidation of G6PD and PHGDH, thus promoting cancer cell proliferation in a manner independent of pyrimidine synthesis. These findings define a mechanism by which a pivotal nucleotide-synthetic enzyme activates central carbon metabolic pathways to support cancer cell proliferation.

RESULTS

Pyrimidine-synthesis-independent activity of CAD in cancer cell proliferation

To probe the roles of CAD in cancer development, we analyzed CAD protein expression and its activation, as indicated by phosphorylation of serine 1859 (pS1859) via the Cancer Proteogenomic Data Analysis Site (cProSite). Compared with tumor-adjacent tissues, the levels of CAD protein and pS1859 are significantly elevated in tumors across all or most of the analyzed tissue types (Figure 1A). To further investigate the roles of CAD in cancer development, we depleted CAD via short hairpin RNAs (shRNAs) in cancer cells (Figure S1A) and examined cell proliferation. CAD depletion nearly abolished the proliferation of breast, liver, and lung cancer cell lines, while reducing proliferation in colorectal cancer cells by ∼50%–70% and in H1648 lung cancer cells by ∼20%–40% (Figure 1B). We then chose two highly sensitive cell lines, HepG2 and MCF7, and one less sensitive cell line, HCT116, to assess the effect of CAD depletion on cancer cell proliferation in nude mice. CAD depletion nearly abolished tumor formation in all cancer cell lines, including the HCT116 cell line, which proliferates despite CAD deletion when cultured *ex vivo* (Figures 1C–1E and S1B). These results show that CAD is critical for the proliferation of most cancer cell lines, particularly *in vivo*.

To determine whether pyrimidine synthetic activity is responsible for the requirement of CAD in cancer cell proliferation, we supplemented CAD-deleted HepG2 cells with uridine or dihydroorotate (DHO) to restore the pyrimidine pool. Cell proliferation analysis showed that CRISPR-Cas9-mediated CAD deletion via two independent sgRNAs abolished cell growth (Figures S1C and S1D), and uridine/DHO supplementation marginally increased the proliferation of CAD-deleted HepG2 cells (Figures 1F, S1E, and S1F). In CAD-deleted HepG2 cells, uridine supplementation fully restored the reduced pyrimidine pool, whereas DHO supplementation rescued intracellular DHO levels without replenishing pyrimidine metabolites (Figure S1G). Metabolite analysis showed that uridine uptake and its conversion to UMP, UDP, and UTP were not impaired by CAD depletion (Figure S1H). Similarly, uridine and DHO supplementation marginally increased the proliferation of CAD-depleted MCF7 cells, even though uridine supplementation fully restored the pyrimidine pool (Figures S1I–S1K). Additionally, UMPS depletion reduced cell proliferation by ∼40% (Figures 1G and S1L–S1N), which was fully restored by uridine supplementation (Figure 1H), in HepG2 and MCF7 cells. These results suggest a pyrimidine synthesis-independent activity of CAD in cancer cell proliferation.

CAD interacts with G6PD and PHGDH and activates the PPP and SSP

We previously reported that CAD deamidates RelA to promote aerobic glycolysis, thus fueling cancer cell proliferation.[27] To determine whether RelA contributes to the essential role of CAD in cancer cell proliferation, we deleted RelA in representative human cancer cell lines and examined cell proliferation. This showed that RelA deletion had no effect on the proliferation of HepG2, MDA-MB-231, and HT29, while significantly reducing the proliferation of Huh7, MCF7, HCT116, and H522 to varying extents (Figures S2A and S2B). Moreover, CAD deletion significantly impaired cell proliferation in RelA-deficient HepG2 and HT29 cells (Figures S2C and S2D). Thus, CAD promotes cell proliferation independently of RelA in some cancer cell lines. To elucidate the underlying mechanism, we identified CAD-interacting proteins for tandem mass spectrometry (MS) using HepG2/FLAG-CAD cells (Figure 2A). We were intrigued by the interaction of CAD with G6PD and PHGDH. To confirm the interaction between CAD and G6PD or PHGDH, we engineered G6PD FLAG knockin (KI) or PHGDH FLAG KI using CRISPR-Cas9 in HepG2 cells. Co-immunoprecipitation showed that CAD was detected with G6PD and PHGDH in these KI HepG2 cell lines (Figures 2B, 2C, S2E, and S2F). To determine the effect of CAD on G6PD and PHGDH, we deleted CAD in G6PD-FLAG KI or PHGDH FLAG KI HepG2 cells and purified G6PD or PHGDH via affinity chromatography for an *in vitro* enzymatic activity assay. We found that CAD deletion reduced the activity of G6PD and PHGDH (Figures 2D and 2E). When metabolites in CAD-deleted HepG2 cells were analyzed by pathway impact, CAD deletion significantly altered metabolites involved in the purine and pyrimidine metabolisms, as well as the PPP, SSP, and one-carbon metabolisms, which correlated with changes in G6PD and PHGDH (Figures 2F, S2G, and S2H). This was further supported by the pool size of selected metabolites (Figure 2G). We then performed tracing experiments with [U-^{13}C]glucose and analyzed heavy isotopologs of 6-phosphogluconate (6PG, m+6) and ribose- or ribulose-5-phosphate (R5P/Ru5P, m+5) of the PPP and serine (m+3) of the SSP (Figure 2H). CAD deletion in HepG2 cells significantly reduced the heavy isotopologs of 6PG, R5P/Ru5P, and serine (Figure 2I). Similar results were obtained in CAD-deleted MCF7 cells (Figures S2I and S2J). To assess the RelA-independent activity of CAD in activating the PPP and SSP, we depleted CAD in RelA-KO MCF7 cells for tracing analysis and found that CAD deletion reduced the heavy isotopologs of 6PG and 3PS (Figures S2K and S2L). Similar effect of CAD deletion was observed in RelA-KO MEFs (Figures S2M and S2N). Collectively, these results demonstrate that CAD activates the PPP and SSP in proliferating cells.

To determine whether the metabolic change by CAD depletion is due to cell toxicity or death, we employed the less sensitive HCT116 cells for CAD deletion and 2-TCPA for transient CAD inhibition.[30] The synthesis of ^{13}C-incorporated 6PG and serine was significantly inhibited in CAD-knockout HCT116 cells compared with that in wild-type cells (Figure S2O). 2-TCPA

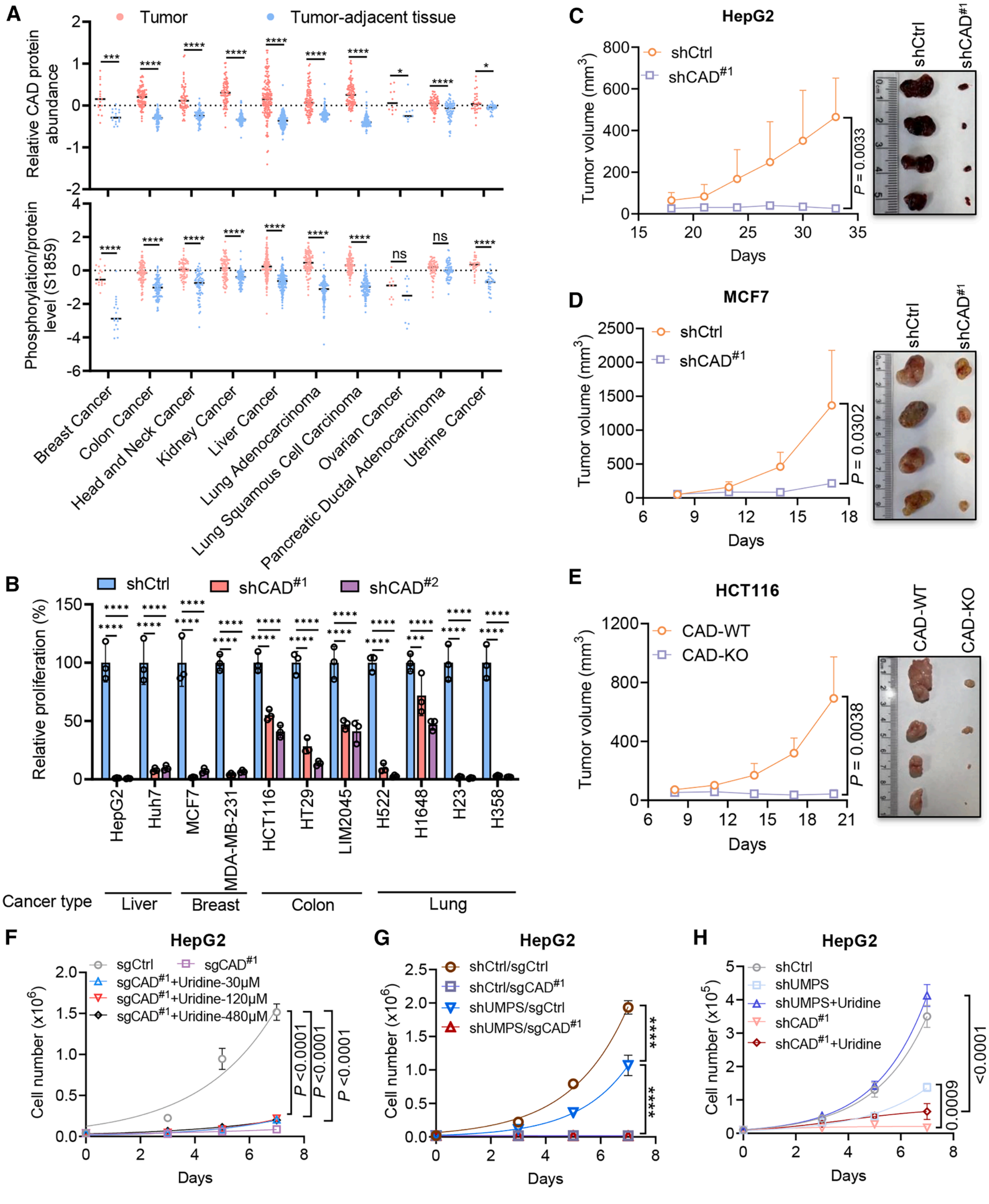

Figure 1. Pyrimidine synthesis-independent activity of CAD in cancer cell proliferation

(A) Levels of total CAD and its S1859 phosphorylated protein in tumors and tumor-adjacent tissues. Data represent mean ± SD. $^{*}p < 0.05$; $^{***}p < 0.001$; $^{****}p < 0.0001$; ns, not significant.

(B) Proliferation of indicated cancer cells with or without CAD depletion. Data represent mean ± SD ($n = 3$). $^{***}p < 0.001$; $^{****}p < 0.0001$.

(C–E) Tumor growth in nude mice transplanted with indicated control or CAD-depleted cancer cells. Data represent mean ± SD ($n = 4$).

(F) Proliferation of control or CAD-deleted HepG2 cells that were supplemented with uridine of indicated concentrations. Data represent mean ± SD ($n = 3$).

(G) Proliferation of HepG2 cells infected with lentivirus carrying non-targeting sgRNA or shRNA (sgCtrl or shCtrl), or that targeting CAD or UMPS (sgCAD or shUMPS). Data represent mean ± SD ($n = 3$). $^{****}p < 0.0001$.

(H) Proliferation of control, UMPS-depleted, or CAD-depleted HepG2 cells that were supplemented with 30 μM uridine. Data represent mean ± SD ($n = 3$).

See also Figure S1.

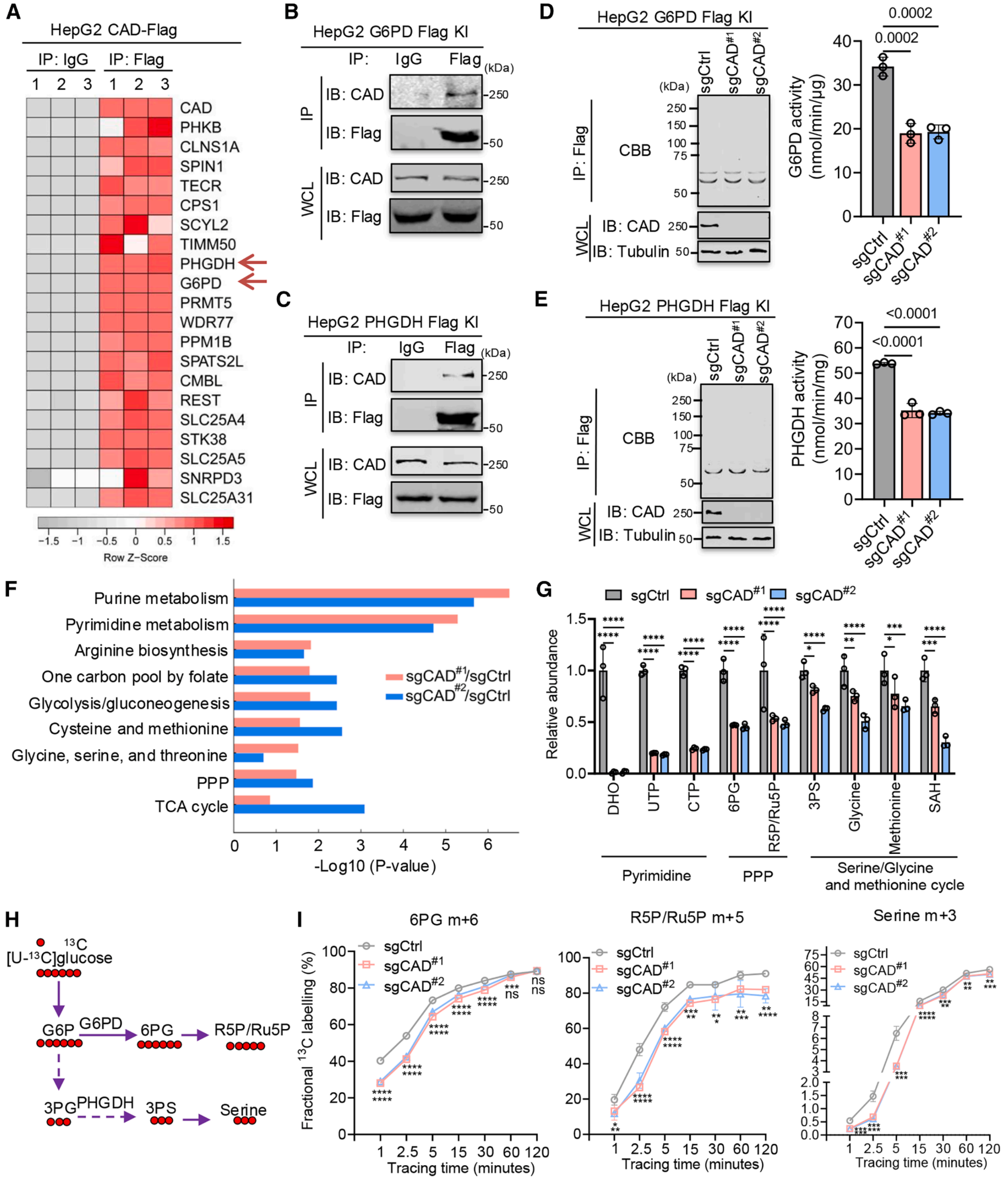

Figure 2. CAD interacts with G6PD and PHGDH and activates the PPP and SSP

(A) CAD-binding proteins in HepG2 cells were identified by affinity chromatography and tandem MS.

(B and C) Immunoblots of precipitated proteins and whole-cell lysates (WCLs) from HepG2/FLAG-G6PD (B) or HepG2/FLAG-PHGDH (C) knockin cells.

(D and E) Coomassie brilliant blue (CBB) staining and enzymatic activities of purified G6PD or PHGDH from knockin cells described in (B) and (C) with or without CAD deletion. Data represent mean ± SD (*n* = 3).

(F) Metabolic pathways that were altered by CAD deletion in HepG2 cells.

(G) Metabolites in indicated pathways between control and CAD-deleted HepG2 cells analyzed by LC-MS. Data represent mean ± SD (*n* = 3).

(H) Diagram of the isotope labeling of selected metabolites of the central carbon metabolism using [U-^{13}C]glucose.

(I) Fraction of the heavy isotopologs of indicated metabolites in control and CAD-deleted HepG2 cells traced with [U-^{13}C]glucose for indicated time points. Data represent mean ± SD (*n* = 3).

See also Figure S2.

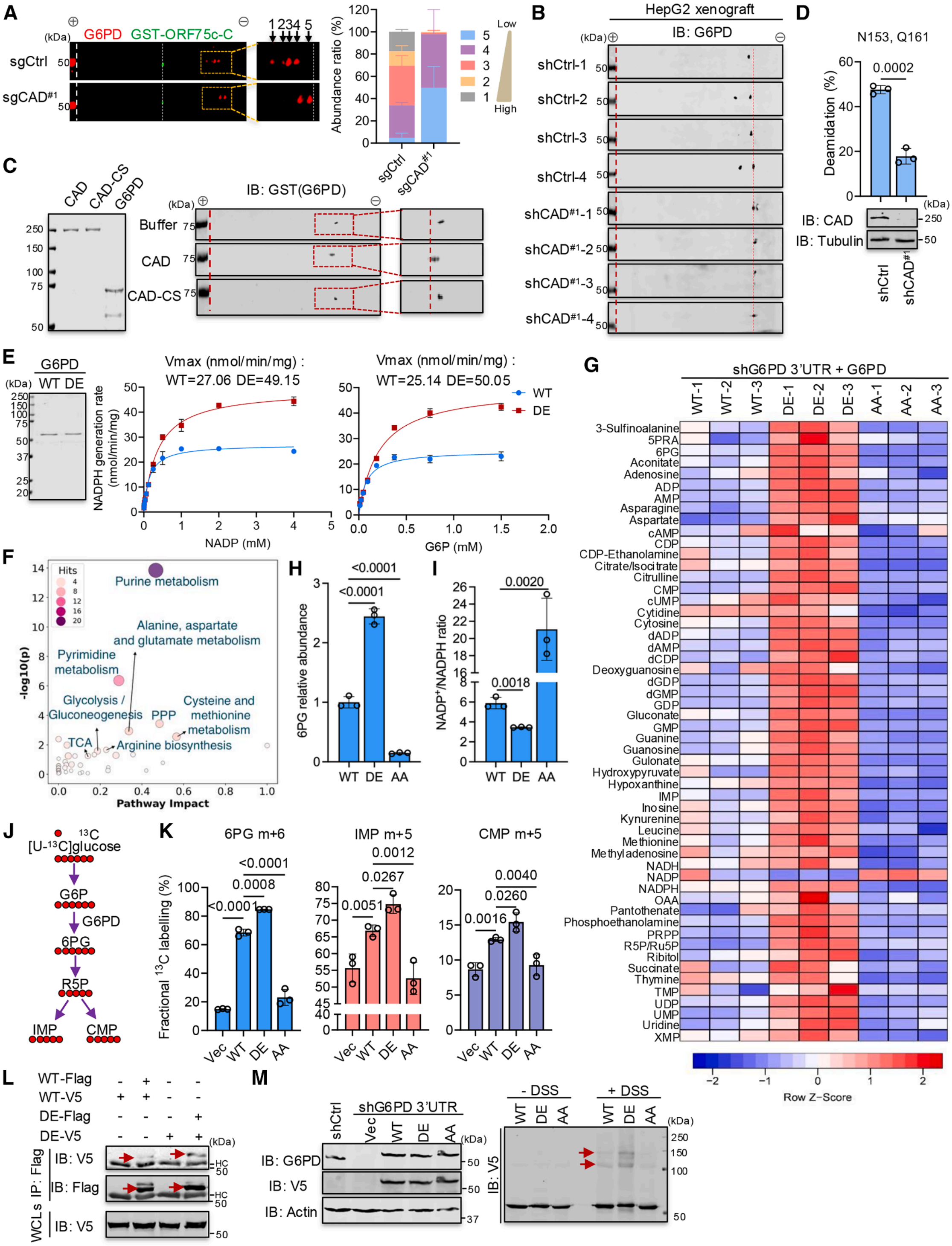

Figure 3. CAD deamidates and activates G6PD to upregulate the PPP

(A) Immunoblots of WCLs of sgCtrl and sgCAD HepG2 cells analyzed by two-dimensional gel electrophoresis (2DGE). A GST fusion containing the C terminus of murine gammaherpesvirus 68 ORF75c was spiked as a reference. The potential deamidation levels of each species are shown in the order from low to high (data represent mean ± SD, *n* = 3).

(B) Immunoblots of lysates of tumors from control or CAD-depleted HepG2 xenograft analyzed by 2DGE.

(C) CBB staining and immunoblots of the *in vitro* deamidation reactions using purified CAD, CAD-CS, and GST-G6PD analyzed by 2DGE.

(legend continued on next page)

reduced the heavy isotopologs of 6PG, R5P/Ru5P, serine, and glycine in a dose-dependent manner in HepG2 cells (Figure S2P). Overall, CAD depletion inhibits the PPP and SSP without apparent cell toxicity.

CAD deamidates and activates G6PD to upregulate the PPP

CAD interacts with G6PD and promotes the activity of the PPP, supporting the hypothesis that CAD deamidates to activate G6PD. We first examined the charge status of G6PD using two-dimensional gel electrophoresis (2DGE) and found that CAD depletion in HepG2 and MCF7 cells shifted G6PD toward the negative end of the gel strip, consistent with its deamidation (Figures 3A, S3A, and S3B). Using tumors derived from xenografted cancer cells in nude mice (Figures 1C and 1D), we found that G6PD charge was significantly increased in tumors derived from CAD-depleted cells compared with those derived from control cells (Figures 3B and S3C). We then purified CAD and the glutaminase-deficient CAD-C252S (CAD-CS) from transfected 293T cells, and GST-G6PD from bacteria for an *in vitro* deamidation assay. We found that CAD, but not the CAD-CS mutant, shifted GST-G6PD toward the positive end of the gel strip (Figure 3C). To identify the sites of deamidation, we purified G6PD with or without CAD overexpression in 293T cells and performed tandem MS analysis. This identified two sites of deamidation, i.e., N153 and Q161 (Figure S3D). When endogenous G6PD in HepG2 cells was analyzed, CAD depletion strikingly decreased the occupancy of deamidated peptides containing N153 or Q161 (Figure 3D). Conversely, CAD significantly increased the abundance of deamidated G6PD peptides *in vitro* (Figure S3E). Moreover, CAD deamidated a synthetic peptide containing N153 and Q161 *in vitro*, whereas the glutaminase-deficient mutant failed to do so (Figure S3F). To determine whether these are the only deamidated sites, we generated a G6PD mutant containing N153D and Q161E mutations, designated as G6PD-DE. When analyzed by 2DGE alongside wild-type G6PD, the G6PD-DE mutant migrated toward the positive end of the gel strip and was not shifted by CAD deletion, whereas wild-type G6PD behaved as expected in HepG2 and MCF7 cells (Figures S3G and S3H). To evaluate the effect of deamidation on the enzymatic activity of G6PD, we purified wild-type G6PD and G6PD-DE for *in vitro* dehydrogenase assays. G6PD-DE demonstrated a maximal velocity (V_{max}) of approximately 2-fold higher than that of wild-type G6PD (Figure 3E), with N153D and Q161E mutations increased G6PD enzymatic activity alone or in combination (Figure S3I). Thus, CAD-mediated deamidation of G6PD activates its dehydrogenase activity in the PPP.

To further validate the enzymatic activity of G6PD-DE, we performed metabolite analysis for the pool size and tracing with [U-^{13}C]glucose using G6PD-depleted HepG2 cells reconstituted with wild-type G6PD, the deamidated G6PD-DE and deamidation-resistant G6PD-AA, which were expressed at levels comparable to endogenous G6PD (Figure S3J). When the pool size of metabolites was analyzed by pathway impact, metabolites altered by G6PD-DE compared with wild-type G6PD clustered into the purine and pyrimidine metabolism, amino acid (including alanine, aspartate, and glutamate) metabolism, arginine synthesis, and PPP (Figures 3F and S3K). In general, G6PD-DE increased, while G6PD-AA decreased, the pool size of metabolites of these pathways compared with wild-type G6PD (Figure 3G). Consistent with the activation of the PPP by deamidation, G6PD-DE elevated, while G6PD-AA reduced 6PG and NADPH compared with wild-type G6PD (Figures 3H and 3I). We further analyzed the activity of the PPP and nucleotide synthesis by tracing with [U-^{13}C]glucose. We found that G6PD-DE increased the synthesis of 6PG, inosine monophosphate (IMP), uridine diphosphate (UDP), and cytidine monophosphate (CMP), whereas G6PD-AA failed to do so (Figures 3J, 3K, and S3L). Similar results were observed for increased heavy isotope-labeled 6PG fraction in G6PD-depleted MCF7 reconstituted with wild-type G6PD, G6PD-DE, and G6PD-AA (Figures S3M and S3N). To query how deamidation regulates G6PD activity, we analyzed the dimerization/oligomerization that activates G6PD. Gel filtration showed that G6PD-DE eluted in fractions of larger molecular weight compared with wild-type G6PD (Figure S3O). Co-immunoprecipitation showed that more G6PD-DE precipitated as dimer/oligomer than wild-type G6PD (Figure 3L). The disuccinimidyl suberate (DSS) crosslinking experiment demonstrated that higher levels of G6PD-DE were captured as dimers/oligomers by DSS than wild-type G6PD, while G6PD-AA showed the opposite phenotype (Figure 3M). Taken together, these results show that deamidation activates G6PD of the PPP to support NADPH generation and *de novo* nucleotide synthesis.

CAD deamidates and activates PHGDH to promote the SSP and one-carbon metabolism

PHGDH catalyzes the first and rate-limiting step of the SSP that supports one-carbon metabolism for fundamental biological

(D) Tandem MS analysis of deamidated peptides containing N153 or Q161 in control or CAD-depleted HepG2/FLAG-G6PD knockin cells. Data represent mean ± SD ($n = 3$).

(E) CBB staining and enzymatic activities of purified G6PD-WT and G6PD-DE. Data represent mean ± SD ($n = 3$).

(F) Altered metabolic pathways between G6PD-depleted HepG2 cells reconstituted with G6PD-WT and G6PD-DE.

(G) A heatmap showing metabolites in G6PD-depleted HepG2 cells reconstituted with wild-type G6PD, G6PD-DE, or G6PD-AA.

(H and I) The relative abundance of 6PG and $NADP^+$/NADPH ratio in HepG2 cells described in (G). Data represent mean ± SD ($n = 3$).

(J) Diagram of the heavy isotopologs of selected metabolites labeled with [U-^{13}C]glucose.

(K) Fractions of heavy isotopologs of indicated metabolites in cells described in (G) that were traced with [U-^{13}C]glucose. Data represent mean ± SD ($n = 3$).

(L) Immunoblots of precipitated proteins and WCLs of G6PD-depleted HepG2 cells reconstituted with G6PD-WT-FLAG and G6PD-WT-V5 or G6PD-DE-FLAG and G6PD-DE-V5.

(M) Immunoblots of extracts of G6PD-depleted HepG2 cells reconstituted with V5-tagged wild-type G6PD, G6PD-DE, or G6PD-AA treated with or without disuccinimidyl suberate (DSS).

See also Figure S3.

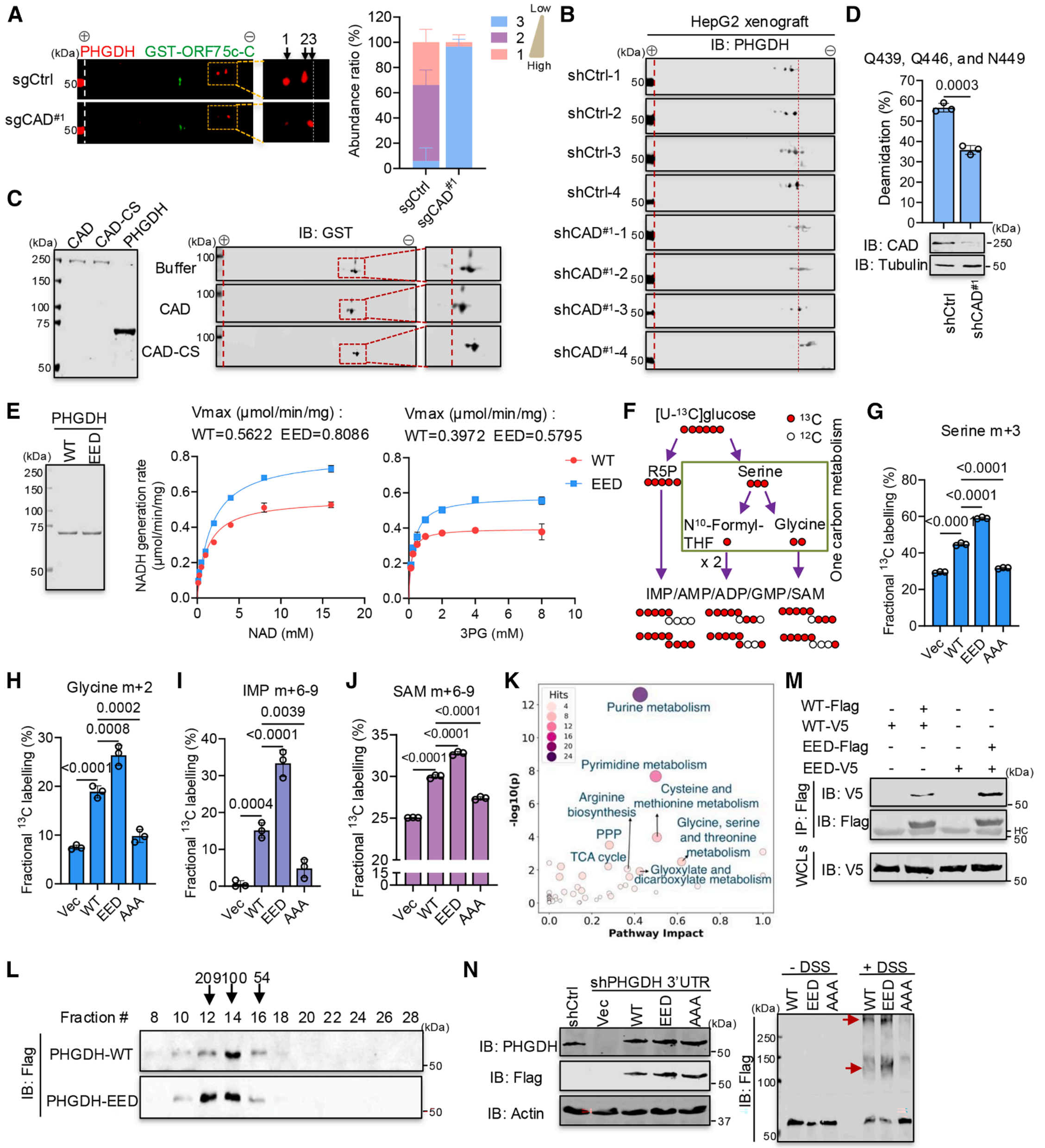

Figure 4. CAD deamidates and activates PHGDH to upregulate the SSP and one-carbon metabolism

(A) Immunoblots of WCLs of control or CAD-depleted HepG2 cells analyzed by 2DGE. A GST fusion containing the C terminal of MHV68 ORF75c was spiked as a reference. The potential deamidation levels of each species are shown in order from low to high. Data represent mean ± SD (*n* = 3).

(B) Immunoblots of lysates of tumors from control or CAD-depleted HepG2 xenograft analyzed by 2DGE.

(C) CBB staining and immunoblots of the *in vitro* deamidation reactions using purified CAD, CAD-CS, and GST-PHGDH analyzed by 2DGE.

(D) Tandem MS analysis of deamidated peptides containing Q439, Q446, or N449 in control or CAD-depleted HepG2/FLAG-PHGDH knockin cells. Data represent mean ± SD (*n* = 3).

(E) CBB staining and the enzymatic activity of purified wild-type PHGDH and deamidated PHGDH-EED. Data represent mean ± SD (*n* = 3).

(F) Diagram of the heavy isotopologs of indicated metabolites labeled with [U-^{13}C]glucose.

(G–J) Fractions of the heavy isotopologs of the indicated metabolites in PHGDH-depleted HepG2 cells reconstituted with Vec, wild-type PHGDH, deamidated PHGDH-EED, or deamidation-resistant PHGDH-AAA traced with [U-^{13}C]glucose. Data represent mean ± SD (*n* = 3).

(K) Top metabolic pathways significantly altered by wild-type PHGDH and PHGDH-AAA in reconstituted HepG2 cells.

(L) Immunoblots of PHGDH in fractions (indicated by numbers) collected after size exclusion chromatography.

(legend continued on next page)

processes.[31] CAD may deamidate and activate PHGDH to promote carbon flux through the SSP. We first assessed the charge status of PHGDH and found that CAD depletion in HepG2 and MCF7 cells abolished the more negatively charged species of PHGDH, consistent with its deamidation (Figures 4A, S4A, and S4B). CAD depletion also increased the charge of PHGDH in xenograft tumors (Figures 4B and S4C). The *in vitro* deamidation assay showed that wild-type CAD, but not CAD-CS, reduced the PHGDH charge (Figure 4C). Next, tandem MS analysis using purified PHGDH with and without CAD overexpression identified three sites, i.e., Q439, Q446, and N449, whose deamidation was elevated by CAD (Figure S4D). In HepG2 cells, the frequency of deamidation at these three sites was lower in CAD-deleted cells than in control cells (Figure 4D). In the *in vitro* assay, CAD markedly elevated the abundance of deamidated PHGDH peptides containing these three identified sites (Figure S4E). To determine the site specificity of CAD-mediated deamidation, we generated a PHGDH mutant containing all three deamidated residues, i.e., Q439/446E, N449D, designated as PHGDH-EED, and examined its charge status. The 2DGE showed that PHGDH-EED migrated to the positive end of the gel strip and CAD depletion shifted wild-type, but not the PHGDH-EED mutant, toward the negative end of the gel strip (Figures S4F and S4G). These results support the conclusion that CAD deamidates PHGDH.

To assess the effect of deamidation on the metabolic activity of PHGDH, we first analyzed the dehydrogenase activity of PHGDH *in vitro* using purified PHGDH. When wild-type PHGDH and PHGDH-EED were compared, the V_{max} of PHGDH-EED was ~1.4-fold higher than that of wild-type PHGDH (Figure 4E). All three deamidation mutations elevated PHGDH activity, and when combined, they did the most (Figure S4H). To evaluate the *in vivo* metabolic activity, we depleted PHGDH in HepG2 cells and reconstituted them with wild-type, the deamidated PHGDH-EED, or the deamidation-resistant PHGDH-AAA mutant (Figure S4I). When these cells were analyzed by tracing with [U-^{13}C]glucose, we found that PHGDH-EED increased the heavy isotopologs of serine and glycine significantly more than wild-type PHGDH. By contrast, PHGDH-AAA had a minimal effect in increasing these labeled metabolites of the SSP (Figures 4F–4H). Similarly, PHGDH-EED increased, while PHGDH-AAA reduced, heavy isotopologs of 3PS compared with wild-type PHGDH in MCF7 cells (Figures S4J and S4K). When analyzed by tracing with [U-^{13}C]glucose, ribose and serine can contribute five and up to four carbons in purines, respectively (Figure 4F). Thus, the abundance of nucleotides containing 6 to 9 heavy carbons, i.e., isotopologs of m+6 to m+9, serves as indicators of PHGDH activity. When isotopologs of IMP were analyzed, we found that PHGDH-EED increased the heavy (m+6 to m+9) fractions, whereas wild-type PHGDH and PHGDH-AAA had only a minimal effect (Figure 4I). The SSP also provides intermediates to maintain the pool of one-carbon metabolites such as S-adenosyl methionine (SAM). When SAM heavy isotopologs were quantified, a similar pattern of activity of PHGDH in SAM synthesis was observed in the order of PHGDH-EED, wild-type PHGDH, and PHGDH-AAA (Figure 4J). Interestingly, PHGDH-EED also resulted in higher labeling of m+6 to m+8 species of UDP, which were heavy isotopologs derived from aspartate, whereas PHGDH-AAA reduced the labeling compared with wild-type PHGDH (Figures S4L and S4M). When metabolites of PHGDH-depleted HepG2 reconstituted with wild-type PHGDH or PHGDH-AAA were compared by pathway impact, we found that highly altered metabolites clustered into pathways of the pyrimidine and purine metabolism, cysteine-methionine metabolism, glycine-serine metabolism, TCA cycle, and glyoxylate and dicarboxylate metabolism (Figures 4K and S4N). The effect of PHGDH deamidation was further supported by the effect of CAD depletion on SAM and nucleotides in HepG2 cells, as analyzed by the pool size and tracing with [U-^{13}C]glucose (Figures S4O–S4Q). To further probe the mechanism by which deamidation impacts the dehydrogenase activity of PHGDH, we analyzed its dimerization/oligomerization by gel filtration, co-immunoprecipitation, and DSS-mediated crosslinking as described for G6PD. These results show that the deamidated PHGDH-EED was more readily detected as dimers or oligomers than wild-type PHGDH (Figures 4L–N). Taken together, these results support the conclusion that deamidation activates PHGDH of the SSP and downstream metabolic pathways.

CAD-mediated deamidation of G6PD and PHGDH promotes cancer cell proliferation

CAD activates the PPP and SSP to fuel biosynthesis and other related pathways likely to empower cancer cell proliferation. When HepG2 cell proliferation was examined by either cell enumeration or carboxyfluorescein succinimidyl ester (CFSE) staining followed by flow cytometry analysis, the deamidation-resistant G6PD-AA and PHGDH-AAA had a minimal effect on cell proliferation compared with wild-type G6PD and PHGDH, whereas the deamidated G6PD-DE and PHGDH-EED proliferated more robustly than wild-type counterparts (Figures 5A and S5A–S5C). A similar pattern was also observed when either G6PD or PHGDH, along with its deamidated and deamidation-resistant mutants, was analyzed in HepG2 cells (Figures S5D and S5E). Additionally, the expression of deamidated G6PD and PHGDH significantly rescued cell proliferation reduced by CAD deletion (Figures S5F and S5G). To further explore the role of CAD-mediated deamidation of G6PD and PHGDH in supporting cancer cell proliferation across additional models, we analyzed the pyrimidine-independent role of CAD in the proliferation of A549, HeLa, HCT116, and A375 cells, along with the charge status of G6PD and PHGDH upon CAD deletion. In A549, HeLa, and HCT116 cells, CAD deletion abolished cell proliferation, and uridine supplementation restored the proliferation

---

(M) Immunoblots of precipitated proteins and WCLs of PHGDH-depleted HepG2 cells reconstituted with wild-type PHGDH or PHGDH-EED that carries FLAG and V5 epitope.

(N) Immunoblots of extracts of PHGDH-depleted HepG2 cells reconstituted with FLAG-tagged wild-type PHGDH, PHGDH-EED, or PHGDH-AAA treated with or without DSS.

See also Figure S4.

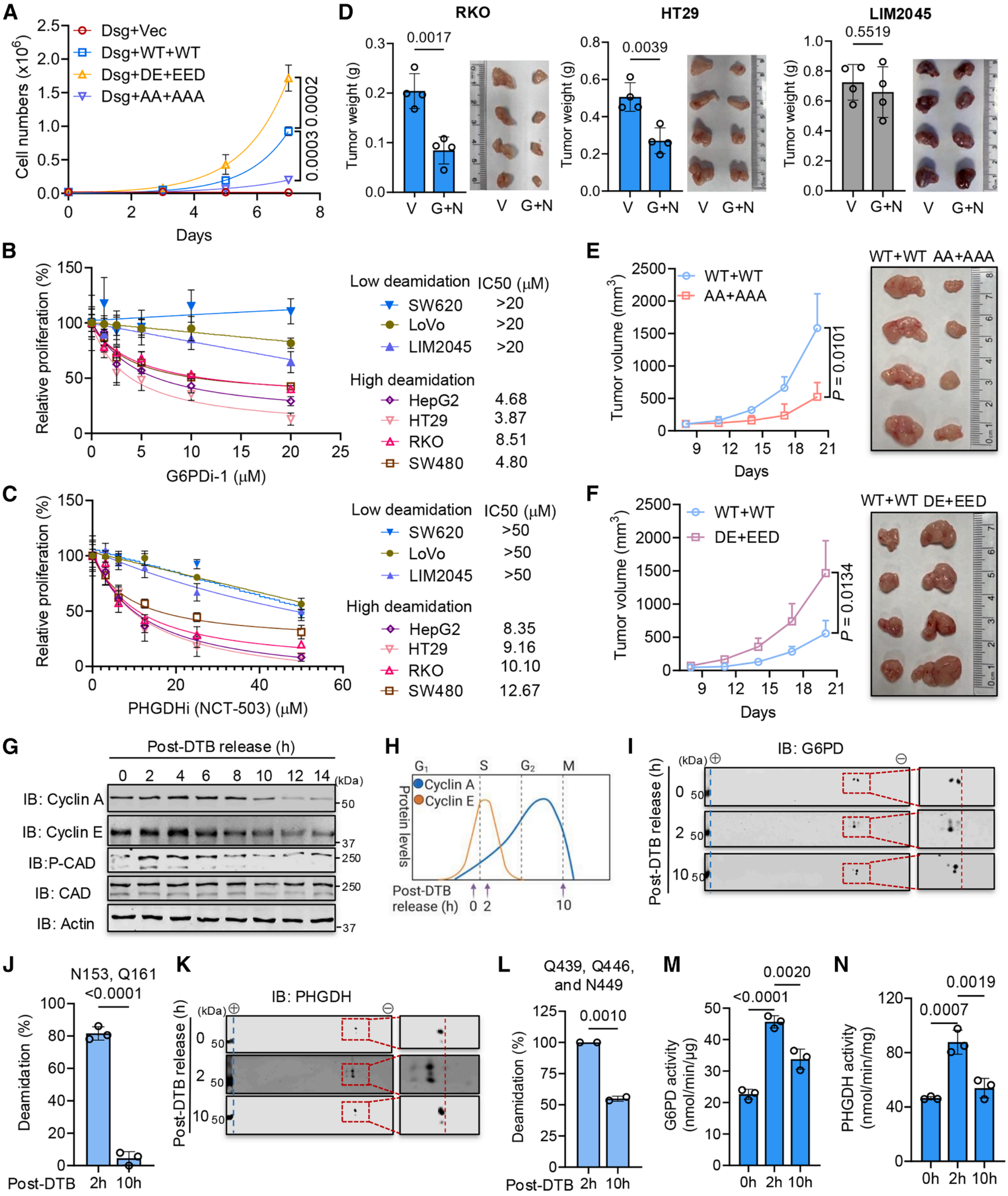

Figure 5. CAD-mediated deamidation of G6PD and PHGDH promotes cancer cell proliferation

(A) Proliferation of double G6PD and PHGDH sgRNAs (Dsg) transduced HepG2 cells reconstituted with Vec, wild-type G6PD and PHGDH, deamidated G6PD-DE and PHGDH-EED, or deamidation-resistant G6PD-AA and PHGDH-AAA. Data represent mean ± SD (*n* = 3).

(B and C) Proliferation of representative human cancer cell lines treated with a G6PD inhibitor (G6PDi-1, B) or a PHGDH inhibitor (NCT-503, C). Data represent mean ± SD (*n* = 3).

(D) Weight and size of tumors developed in nude mice transplanted with RKO, HT29, and LoVo colorectal cancer cells, treated with vehicle (V) or G6PDi-1 plus NCT-503 (G + N) (10 mg/kg). Data represent mean ± SD (*n* = 4).

(E and F) Tumor growth in nude mice transplanted with G6PD- and PHGDH-depleted HT29 or LoVo cells reconstituted with wild-type G6PD and PHGDH, G6PD-AA and PHGDH-AAA, or G6PD-DE and PHGDH-EED. Data represent mean ± SD (*n* = 4).

(G) Immunoblots of WCLs of HepG2 cells at indicated time points after release from double thymidine blockade (DTB).

(H) Diagram showing the distinct cell-cycle phases marked by corresponding cyclin expression and time points after DTB.

(I and K) Immunoblots of WCLs of HepG2 cells at indicated time points post DTB analyzed by 2DGE.

(legend continued on next page)

to varying degrees but failed to reach that of control cells (Figures S5H–S5K). LC-MS analysis of these three cell lines showed that uridine supplementation in CAD-deleted cells effectively restored pyrimidine pools, supporting the normal functionality of uridine uptake and salvage synthesis (Figures S5M–S5O). CAD deficiency in these three cell lines caused G6PD and PHGDH to shift toward the negative end of the gel strip, consistent with reduced deamidation (Figures S5P and S5Q). Interestingly, high-dose (480 μM) uridine nearly restored the proliferation of CAD-deleted cells to the levels comparable to wild-type A375 cells (Figures S5H and S5L). PHGDH deamidation was only marginally reduced, whereas G6PD deamidation remained unaffected, by CAD deletion in A375 cells (Figure S5Q). These results further support a pyrimidine-independent function of CAD in promoting cancer cell proliferation (such as A549, HCT116, and HeLa), while also highlighting cancer cells (e.g., A375), whose proliferation solely depends on the pyrimidine synthetic activity of CAD. Collectively, CAD deamidates G6PD and PHGDH to promote cancer cell proliferation.

To assess the biological significance of G6PD and PHGDH deamidation, we determined the inhibitory concentration of 50% (IC50) of their known inhibitors using cancer cell lines of high and low deamidation. Within a panel of seven cancer cell lines with comparable G6PD and PHGDH expression, we found that RKO, SW480, HT29, and HepG2 demonstrated higher deamidation of G6PD and PHGDH than LoVo, SW620, and LIM2045 (Figures S6A and S6B). When treated with a G6PD inhibitor, G6PDi-1, LoVo, SW620, and LIM2045 cells had an IC50 of >20 μM, whe reasRKO, SW480, HT29, and HepG2 cells had an IC50 of ∼4–10 μM (Figure 5B). Similarly, cancer cell lines with high and low deamidation had an IC50 of ∼10 μM and >50 μM for the PHGDH inhibitor NCT-503, respectively (Figure 5C). G6PDi-1 and NCT-503 together more effectively reduced the proliferation of cancer cells of high deamidation than those of low deamidation, particularly within a lower dose range (Figure S6C). G6PDi-1 and NCT-503 inhibited wild-type and deamidated enzymes with similar IC50, indicating that the enhanced sensitivity of high deamidation cells to the inhibitor arises from their higher dependency on G6PD and PHGDH activity or from other mechanisms that influence inhibitor-binding to deamidated enzymes (Figures S6D and S6E). In nude mice, combined treatment with both inhibitors reduced the growth rate of tumors derived from high deamidation cells (RKO and HT29) by ∼50% (Figures 5D and S6F). The same treatment had no significant effect on the growth or weight of tumors of low deamidation cells (LIM2045). Next, we reconstituted G6PD- and PHGDH-depleted HT29 or LoVo cells, with wild-type or the mutants to examine their proliferation *in vivo* (Figure S6G). This showed that the deamidation-resistant G6PD-AA and PHGDH-AAA inhibited tumor growth, while the deamidated G6PD-DE and PHGDH-EED accelerated tumor growth by ∼3-fold compared with their wild-type counterparts (Figures 5E and 5F). These results show that the deamidation of G6PD and PHGDH promotes cancer cell proliferation.

Because CAD is highly active in the S phase, we profiled the deamidation of G6PD and PHGDH in the cell cycle. When HepG2 cells were synchronized using double thymidine blockade, activated CAD, indicated by S1859 phosphorylation peaked at 2 and 4 h after release from double thymidine treatment, corresponding to the S phase as analyzed by the expression of cyclin A and E (Figures 5G and 5H). In parallel with CAD activation, nearly complete and minimal deamidation of G6PD and PHGDH were observed at 2 and 10 h after double thymidine treatment, respectively (Figures 5I–5L). Similar results for G6PD and PHGDH deamidation were observed in cells of S phase with lovastatin treatment (Figures S6H and S6I). To further corroborate with the cell-cycle-dependent deamidation of G6PD and PHGDH, we purified G6PD and PHGDH from cells at 2 and 10 h after release from double thymidine treatment of FLAG knockin HepG2 cells and performed an *in vitro* dehydrogenase assay (Figures S6J and S6K). This analysis showed that G6PD and PHGDH isolated from S phase cells demonstrated ∼2-fold higher activity than in cells arrested in G1 phase, whereas the activity of both enzymes decreased at 10 h post-double thymidine treatment (Figures 5M and 5N). These results show that CAD deamidates and activates G6PD and PHGDH in the S phase.

The GLN domain of CAD deamidates G6PD and PHGDH and promotes cancer cell proliferation

CAD deamidates G6PD and PHGDH to promote biosynthesis and cancer cell proliferation. However, CAD also fuels cancer cell proliferation in a pyrimidine-synthesis-independent manner. These results prompted us to test whether the GLN domain can promote cancer cell proliferation. Using CAD-deleted HepG2 cells reconstituted with GLN or the glutaminase-deficient GLN-C252S (GLN-CS) mutant, we found that GLN, but not the GLN-CS mutant, restored the proliferation of CAD-deleted cells by ∼50% when cells were supplemented with uridine (30 μM) (Figures 6A and S7A). When supplemented with DHO (50 μM), GLN also restored the proliferation of CAD-deleted HepG2 cells to ∼30% of that of control cells (Figure S7B). Further 2DGE analysis showed that exogenously expressed GLN, but not the GLN-CS mutant, shifted G6PD and PHGDH toward the positive end of the gel strip, consistent with their deamidation (Figure 6B). The exogenously expressed GLN, but not the GLN-CS mutant, elevated the proliferation of LoVo cells by >2-fold in 6 days, which also correlated with the charge reduction of G6PD and PHGDH (Figures 6C, 6D, and S7C). In nude mice, GLN-expressing LoVo cells developed tumors that were 2.5-fold larger in volume compared to those derived from the control cells (Figures 6E and S7D). Moreover, GLN interacts with endogenous G6PD and PHGDH as analyzed by co-immunoprecipitation using stable LoVo/V5-GLN cells (Figures 6F and 6G). *In vitro* deamidation assay showed that GLN, but not GLN-CS, shifted G6PD and PHGDH toward the positive end of the gel strip, supporting their deamidation by GLN (Figure 6H). G6PD and PHGDH, purified from the GLN-expressing cells, demonstrated ∼50% more

---

(J and L) MS analysis of G6PD or PHGDH deamidation occupancies in HepG2 cells at indicated time points after DTB. Data represent mean ± SD (J, *n* = 3; L, *n* = 2).
(M and N) The enzymatic activity of G6PD and PHGDH purified from corresponding knockin cells at indicated time points after released from DTB. Data represent mean ± SD (*n* = 3).
See also Figures S5 and S6.

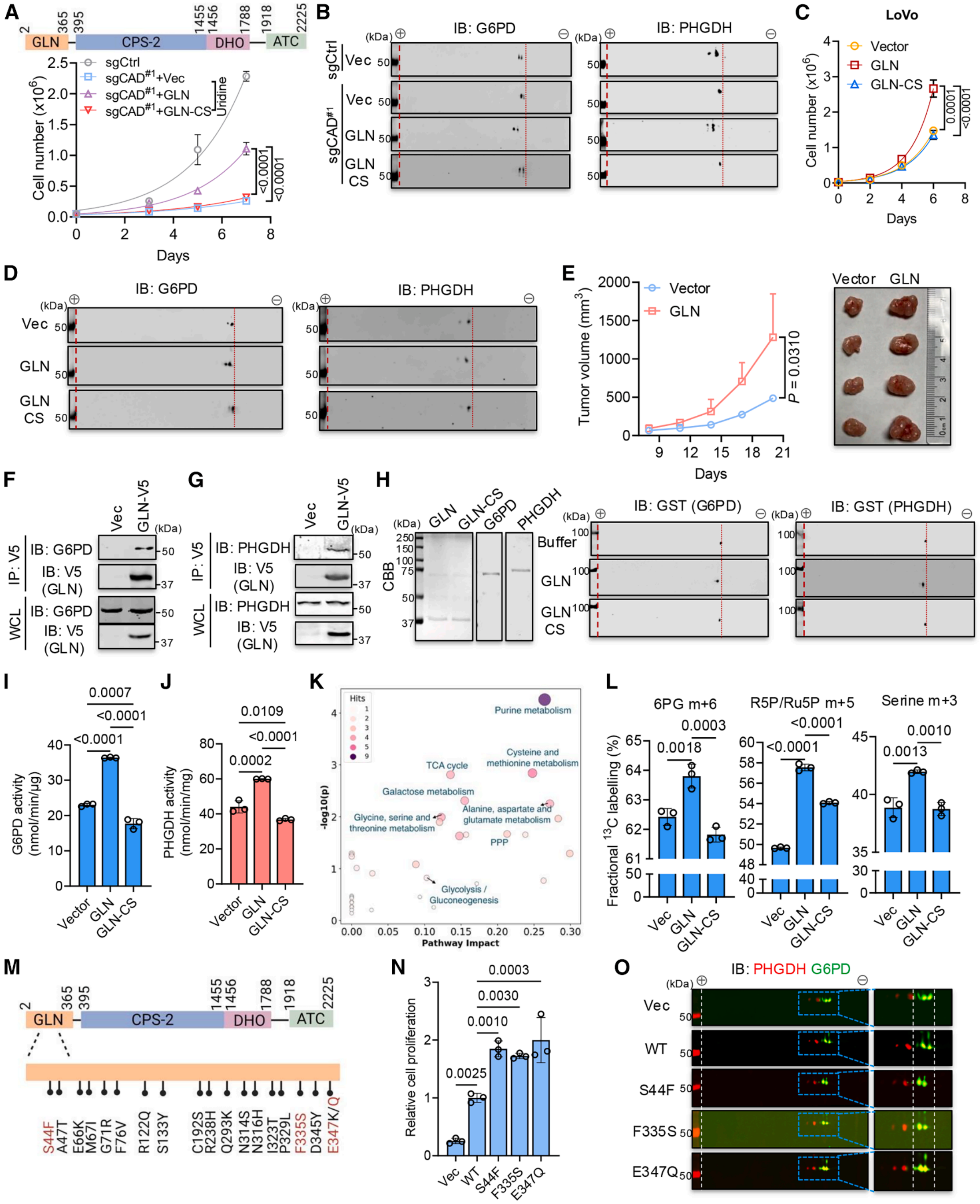

Figure 6. The GLN domain of CAD deamidates G6PD and PHGDH and promotes cancer cell proliferation

(A) Proliferation of CAD-deleted HepG2 cells reconstituted with Vec, GLN, or GLN-CS supplemented with uridine (30 μM). Data represent mean ± SD (*n* = 3).

(B) Immunoblots of WCLs of HepG2 cells as described in (A) analyzed by 2DGE.

(C) Proliferation of LoVo cells stably expressing Vec, GLN, or GLN-CS. Data represent mean ± SD (*n* = 3).

(D) Immunoblots of WCLs of LoVo cells described in (C) after 2DGE.

(E) Tumor growth in nude mice transplanted with LoVo cells with or without exogenous GLN expression. Data represent mean ± SD (*n* = 4).

(F and G) Immunoblots of precipitated proteins and WCLs of LoVo cells stably expressing Vec or GLN.

(H) CBB staining and immunoblots of *in vitro* deamidation reactions using purified GLN, GLN-CS, GST-G6PD, and GST-PHGDH analyzed by 2DGE.

(I and J) The enzymatic activity of G6PD and PHGDH purified from corresponding LoVo knockin cells stably expressing Vec, GLN, or GLN-CS. Data represent mean ± SD (*n* = 3).

(K) Metabolic pathways that were altered in LoVo cells stably expressing Vec or GLN.

(legend continued on next page)

enzymatic activity than their equivalents purified from control cells (Figures 6I, 6J, S7E, and S7F). The metabolite profiling showed that GLN expression significantly altered metabolites of the PPP, SSP, and related pathways (Figure 6K). Heatmap showed that GLN elevated metabolites of the PPP and SSP, e.g., glycine and R5P/Ru5P (Figure S7G). Tracing analysis with [U-^{13}C]glucose demonstrated that GLN, but not the GLN-CS mutant, increased the heavy isotopologs of 6PG, R5P/Ru5P, and serine (Figure 6L). Thus, the GLN domain of CAD can activate G6PD and PHGDH to promote cell proliferation.

When CAD mutations within the human cancer database were examined, we observed that ∼25% of cancer-associated mutations clustered within the GLN domain (Figure 6M). We thus leveraged RelA-mediated NF-κB activation as a proxy to screen for mutations that alter the deamidase activity of CAD. NF-κB luciferase assay identified three mutations that more potently reduced NF-κB activation than wild-type GLN, i.e., S44F, F335S, and E347Q (Figures S7H–S7J), suggesting that these mutations elevate GLN-mediated RelA deamidation. When cell proliferation was examined, we observed that these GLN mutants more robustly elevated the proliferation of LoVo cells than wild-type GLN (Figure S7K). When G6PD and PHGDH were examined by 2DGE, the GLN-S44F and -E347Q mutants more robustly shifted G6PD toward the positive end of the gel strip than wild-type GLN, while all three mutants similarly shifted so toward PHGDH (Figure S7L). F335S showed a minor effect on G6PD charge, which is consistent with its subtle effect on cell proliferation. We then generated CAD mutants containing these mutations and introduced them into CAD-depleted LoVo cells (Figure S7M). All three mutants nearly doubled the proliferation of LoVo cells compared with wild-type CAD (Figure 6N), which correlated with more robust charge reduction of G6PD and PHGDH (Figure 6O). Finally, when purified CAD mutants were used for *in vitro* glutaminase assay, we found that all CAD mutants demonstrated a higher V_{max} than that of wild-type CAD (Figures S7N and S7O). These results characterize cancer-associated mutations within CAD that enhance the deamidation of G6PD and PHGDH to promote cell proliferation.

CAD activation correlates with the deamidation of G6PD and PHGDH in human hepatocellular carcinoma

To further explore the roles of CAD in carcinogenesis, we analyzed the survival of cancer patients in relation to their CAD protein levels via CPPA (Cancer Proteome and Phosphoproteome Atlas)[32] and found that CAD protein expression significantly and inversely correlated with the survival of human hepatocellular carcinoma (HCC) patients, but not with other cancer types (Figures 7A and S8A–S8F). High CAD mRNA expression is also associated with reduced survival based on a The Cancer Genomic Atlas (TCGA) liver cancer dataset (Figure 7B). Within the top 300 proteins associated with the poor prognosis of HCC, CAD ranks number three (Figure 7C). These data implicate a pathogenic role of CAD in HCC. Next, we extended our studies using HCC patient tissues. With a total of 8 paired tumor and tumor-adjacent tissues, we first profiled metabolites of the central carbon metabolism. Glycolytic intermediates, such as G6P/F6P, 6PG, 3PG/2PG, and 3PS, were higher in the tumor tissues than tumor-adjacent tissues (Figure 7D). By contrast, metabolites of the TCA cycle in tumors were either equivalent or lower than those in tumor-adjacent tissues. Furthermore, immunoblotting analysis indicated that CAD expression was higher in four tumors than their tumor-adjacent tissues, whereas all eight tumors had higher levels of pS1859 of CAD than their tumor-adjacent tissues (Figures 7E and S8G). Consistent with CAD activation, elevated levels of charge reduction of G6PD and PHGDH were apparent in tumor tissues compared with tumor-adjacent tissues, suggesting higher deamidation of G6PD and PHGDH in HCC (Figures 7F and S8H). Taken together, these results show that CAD is highly activated, which correlates with the deamidation and activation of G6PD and PHGDH in HCC.

DISCUSSION

De novo nucleotide synthesis is essential for cell proliferation despite the fact most nucleobases are recovered via salvage pathways.[6] Testimony to the essential role of nucleotide synthesis, drugs developed for antitumor and antiviral therapy often target nucleotide-synthetic enzymes or act as nucleotide/nucleoside analogs.[33] CAD and pyrophosphate amidotransferase (PPAT) catalyze a rate-limiting step of the *de novo* synthesis of pyrimidine and purine, respectively.[34] Though CAD and other metabolic enzymes are well defined as executors of cellular metabolism, little is known about whether these enzymes can function as master regulators. Here, we report that activated CAD deamidates G6PD and PHGDH to upregulate the PPP and SSP that promote cancer cell proliferation, respectively. Previous studies demonstrated that glycolytic enzymes, such as phosphofructokinase/fructo-bisphosphatase 4 (PFKFB4), PFKL, PKM2, and HK2, can modify proteins in addition to small-molecule metabolites.[35–38] In addition to G6PD and PHGDH, CAD can deamidate RelA, which shunts RelA from mediating an inflammatory response to aerobic glycolysis, supporting cancer cell proliferation.[27] These studies collectively support the corollary that metabolic enzymes can choreograph cellular metabolic program via "moonlighting" enzymatic activities toward proteins.

CAD is a trifunctional enzyme that consists of CPSase, ATCase, DHOase, and a GLN domain.[39] GLN is presumed to hydrolyze glutamine and provides ammonia for carbamoyl-phosphate synthesis, and the GLN function was shown to be dispensable

---

(L) Fraction of heavy isotopologs of indicated metabolites in LoVo cells stably expressing Vec, GLN, or GLN-CS that were traced with [U-^{13}C]glucose. Data represent mean ± SD ($n = 3$).

(M) A diagram of the structural domains of CAD and cancer-associated mutations within the GLN domain.

(N) Proliferation of CAD-depleted LoVo cells reconstituted with Vec, wild-type CAD, or CAD mutants containing indicated mutations. Data represent mean ± SD ($n = 3$).

(O) Immunoblots of WCLs of LoVo cells as described in (N) analyzed by 2DGE.

See also Figure S7.

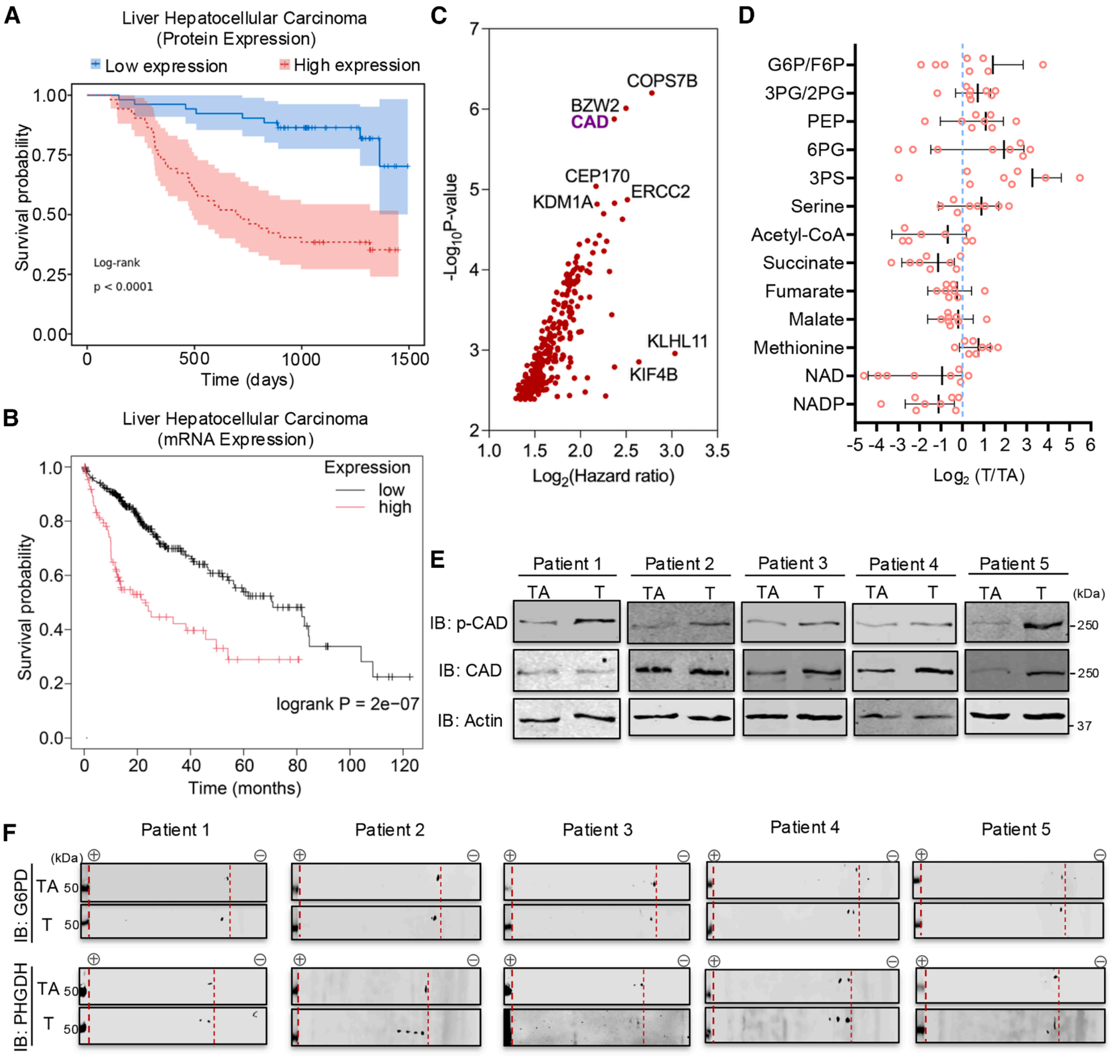

Figure 7. CAD activation correlates with deamidation of G6PD and PHGDH in human hepatocarcinoma

(A) Survival estimate curve for liver cancer patients ranked by the level of total CAD protein.

(B) Survival estimate curve for TCGA liver HCC patients ranked by expression of CAD.

(C) Top 300 proteins associated with the poor prognosis of liver cancer patients were shown by a volcano plot.

(D) Relative abundance of selected metabolites in liver tumors (Ts) and tumor-adjacent tissues (TAs). Data represent mean ± SD (*n* = 8).

(E and F) Immunoblots of lysates of liver tumors (Ts) and tumor-adjacent tissues (TAs) analyzed by immunoblotting with antibodies to CAD and S1859 phosphorylated CAD (E), or 2DGE and immunoblotting with antibodies to G6PD and PHGDH (F).

See also Figure S8.

for pyrimidine synthesis under certain conditions.[40,41] Intriguingly, ∼25% of cancer-associated mutations reside within the GLN domain that accounts for ∼15% of the full-length CAD, suggesting that the GLN domain is under positive selection in cancer cell evolution. In this study, we demonstrate that the GLN domain is sufficient to activate the PPP and SSP via deamidating G6PD and PHGDH, which fuels macromolecule synthesis and cancer cell proliferation. Importantly, several mutations within the GLN domain elevated the deamidase activity of CAD in cell proliferation. The conclusion of the GLN domain capable of hydrolyzing glutamine and deamidating proteins agrees with the fact that the four enzymatic domains of CAD are expressed separately in microorganisms, implying their ancient roles in biological processes beyond pyrimidine synthesis.[12,17] Notably, cancer cell lines display differential reliance on the deamidase activity of CAD, although all cancer cells require pyrimidine synthesis, either *de novo* or salvage, to support their proliferation. For example, CAD-KO melanoma A375 cells can proliferate as efficiently as wild-type cells when supplemented with uridine, indicating that the deamidase activity of CAD is fully dispensable. On the other end, CAD-KO MCF7 and HepG2 cells fail to proliferate when supplemented with uridine, which fully restores nucleotide pools, reflecting the necessity of CAD-mediated protein deamidation. Conceivably, many cancer cells fall within these two extremities. For a few CAD-knockout cells that we tested, we found that uridine supplementation restored pyrimidine pools for all of them, suggesting that most cancer cells have functional salvage nucleotide synthesis pathways.

In addition to *de novo* nucleotide synthesis, the G6PD-catalyzed PPP provides ribose that can shunt carbon resources back to the glycolytic or gluconeogenic pathway.[42] The PPP also produces NADPH, the major reducing power for lipid synthesis.[8,42,43] G6PD is upregulated in diverse cancers, and post-translational modifications such as acetylation and phosphorylation play crucial roles in controlling its activity.[44–46] The CAD-mediated deamidation of G6PD adds another modification to the regulatory mechanism governing metabolic enzyme activation, specifically by inducing dimerization/oligomerization. Similarly, PHGDH catalyzes the first rate-limiting reaction of the SSP, offering serine and other related metabolites for the synthesis of nucleotides and lipids, and replenishing the one-carbon pool that supports methylation of nucleic acids and proteins.[47–49] In this way, PHGDH-mediated metabolism of 3-phosphoglycerate touches upon diverse fundamental biological processes beyond metabolic reprogramming via transcription, translation, and post-translational modifications in signal transduction.[50–53] Indeed, cancer cells explore PHGDH to connect the SSP with one-carbon metabolism and TCA cycle.[31,54,55] Inhibiting PHGDH potently impedes the proliferation of cancer cells *ex vivo* and in xenograft mouse models, supporting the cell-intrinsic activity of metabolic enzymes in tumor formation.[54,56,57] Thus, targeting these metabolic master regulators such as CAD, G6PD, and PHGDH for inhibition promises effective antitumor therapy.

Limitations of the study

Although CAD-mediated deamidation of G6PD and PHGDH plays pivotal roles in cancer cell proliferation, it may not fully account for the pyrimidine-synthesis-independent function of CAD. Additional mechanisms may exist and warrant further investigation. The structural basis by which CAD recognizes and catalyzes G6PD/PHGDH deamidation, and whether specific modifications can alter CAD's substrate preference for small molecules or proteins remain unanswered. Finally, the therapeutic potential of inhibiting CAD or G6PD and PHGDH in immunocompetent individuals hinges on avoiding collateral damage to immune response.

RESOURCE AVAILABILITY

Lead contact

Requests for further information and resources should be directed to and will be fulfilled by the lead contact, Pinghui Feng (pinghuif@usc.edu and FengP@ccf,org).

Materials availability

Plasmids and cell lines generated in this study will be made available upon request, with the approval of the material transfer agreement.

Data and code availability

The MS proteomic data have been deposited in the ProteomeXchange Consortium via the PRIDE partner repository with the dataset identifiers PRIDE: PXD052153, PXD052165, PXD055217, PXD064420. Metabolomic data have been deposited in MetaboLights: MTBLS13498. Unprocessed gels and blots were deposited in Mendeley Data: https://www.doi.org/10.17632/85tsr8c2h8.1. Any additional information required to reanalyze the data reported in this paper is available from the lead contact upon request.

ACKNOWLEDGMENTS

We thank Dr. Santiago Ramón-Maiques (Instituto de Biomedicina de Valencia, Spain) for valuable discussion regarding CAD structure, and Ms. Linda Hattemer for proofreading the manuscript. This study is supported partly by a startup fund from Herman Ostrow School of Dentistry, grants from National Institutes of Health (USA) (CA285192, AI180537, AI184716, and AG070904) and Infectious Disease Society of America Foundation (Microbial Pathogenesis).

AUTHOR CONTRIBUTIONS

Conceptualization, P.F. and C.Q.; investigation, C.Q., Z.A., S.F., X.X., A.C.S., and T.X.; data analyses, C.Q. and W.F.; writing—original draft, P.F. and C.Q.; writing—review & editing, P.F., C.Q., C.B., and T.S.; funding acquisition, P.F.; resources, P.F., T.S., and C.B.

DECLARATION OF INTERESTS

C.B. is a chief scientific advisor of ChromaDex and a co-founder of Alphina Therapeutics.

STAR★METHODS

Detailed methods are provided in the online version of this paper and include the following:

- KEY RESOURCES TABLE
- EXPERIMENTAL MODEL AND STUDY PARTICIPANT DETAILS
  - ○ Cells
  - ○ Clinical samples
  - ○ Mice
  - ○ Plasmids
- METHOD DETAILS
  - ○ Production of lentivirus or retrovirus
  - ○ Construction of gene knockdown, gene-deleted, Flag knockin, and reconstituted cell lines
  - ○ Cell proliferation assay
  - ○ Carboxyfluorescein succinimidyl ester (CFSE) staining
  - ○ Xenograft nude mouse model
  - ○ Two-dimensional gel electrophoresis
  - ○ Metabolite profiling and isotope tracing
  - ○ Protein expression and purification
  - ○ Co-immunoprecipitation (co-IP) and immunoblotting
  - ○ Crosslinking assay
  - ○ In vitro deamidation assay
  - ○ Size exclusion chromatography
  - ○ Cell cycle synchronization
  - ○ Glutaminase assay
  - ○ Dual-luciferase reporter assay
  - ○ G6PD and PHGDH enzymatic assay
  - ○ Proteomics
  - ○ Data mining
- QUANTIFICATION AND STATISTICAL ANALYSIS

SUPPLEMENTAL INFORMATION

Supplemental information can be found online at https://doi.org/10.1016/j.molcel.2026.03.016.

Received: December 27, 2024
Revised: June 19, 2025
Accepted: March 16, 2026
Published: April 7, 2026

REFERENCES

1. Feitelson, M.A., Arzumanyan, A., Kulathinal, R.J., Blain, S.W., Holcombe, R.F., Mahajna, J., Marino, M., Martinez-Chantar, M.L., Nawroth, R., Sanchez-Garcia, I., et al. (2015). Sustained proliferation in cancer: Mechanisms and novel therapeutic targets. Semin. Cancer Biol. *35*, S25–S54. https://doi.org/10.1016/j.semcancer.2015.02.006.
2. Evan, G.I., and Vousden, K.H. (2001). Proliferation, cell cycle and apoptosis in cancer. Nature *411*, 342–348. https://doi.org/10.1038/35077213.
3. Martinez-Outschoorn, U.E., Peiris-Pagés, M., Pestell, R.G., Sotgia, F., and Lisanti, M.P. (2017). Cancer metabolism: a therapeutic perspective. Nat. Rev. Clin. Oncol. *14*, 11–31. https://doi.org/10.1038/nrclinonc.2016.60.
4. Fritz, V., and Fajas, L. (2010). Metabolism and proliferation share common regulatory pathways in cancer cells. Oncogene *29*, 4369–4377. https://doi.org/10.1038/onc.2010.182.
5. Xiao, Y., Yu, T.J., Xu, Y., Ding, R., Wang, Y.P., Jiang, Y.Z., and Shao, Z.M. (2023). Emerging therapies in cancer metabolism. Cell Metab. *35*, 1283–1303. https://doi.org/10.1016/j.cmet.2023.07.006.
6. Mullen, N.J., and Singh, P.K. (2023). Nucleotide metabolism: a pan-cancer metabolic dependency. Nat. Rev. Cancer *23*, 275–294. https://doi.org/10.1038/s41568-023-00557-7.
7. Shi, D.D., Savani, M.R., Abdullah, K.G., and McBrayer, S.K. (2023). Emerging roles of nucleotide metabolism in cancer. Trends Cancer *9*, 624–635. https://doi.org/10.1016/j.trecan.2023.04.008.
8. Patra, K.C., and Hay, N. (2014). The pentose phosphate pathway and cancer. Trends Biochem. Sci. *39*, 347–354. https://doi.org/10.1016/j.tibs.2014.06.005.
9. Yang, M., and Vousden, K.H. (2016). Serine and one-carbon metabolism in cancer. Nat. Rev. Cancer *16*, 650–662. https://doi.org/10.1038/nrc.2016.81.
10. Keibler, M.A., Wasylenko, T.M., Kelleher, J.K., Iliopoulos, O., Vander Heiden, M.G., and Stephanopoulos, G. (2016). Metabolic requirements for cancer cell proliferation. Cancer Metab. *4*, 16. https://doi.org/10.1186/s40170-016-0156-6.
11. Shoaf, W.T., and Jones, M.E. (1973). Uridylic acid synthesis in Ehrlich ascites carcinoma. Properties, subcellular distribution, and nature of enzyme complexes of the six biosynthetic enzymes. Biochemistry *12*, 4039–4051. https://doi.org/10.1021/bi00745a004.
12. Del Caño-Ochoa, F., Moreno-Morcillo, M., and Ramón-Maiques, S. (2019). CAD, A Multienzymatic Protein at the Head of de Novo Pyrimidine Biosynthesis. Subcell. Biochem. *93*, 505–538. https://doi.org/10.1007/978-3-030-28151-9_17.
13. Robitaille, A.M., Christen, S., Shimobayashi, M., Cornu, M., Fava, L.L., Moes, S., Prescianotto-Baschong, C., Sauer, U., Jenoe, P., and Hall, M.N. (2013). Quantitative phosphoproteomics reveal mTORC1 activates de novo pyrimidine synthesis. Science *339*, 1320–1323. https://doi.org/10.1126/science.1228771.
14. Ben-Sahra, I., Howell, J.J., Asara, J.M., and Manning, B.D. (2013). Stimulation of de novo pyrimidine synthesis by growth signaling through mTOR and S6K1. Science *339*, 1323–1328. https://doi.org/10.1126/science.1228792.
15. Graves, L.M., Guy, H.I., Kozlowski, P., Huang, M., Lazarowski, E., Pope, R.M., Collins, M.A., Dahlstrand, E.N., Earp, H.S., 3rd, and Evans, D.R. (2000). Regulation of carbamoyl phosphate synthetase by MAP kinase. Nature *403*, 328–332. https://doi.org/10.1038/35002111.
16. Li, G., Li, D., Wang, T., and He, S. (2021). Pyrimidine Biosynthetic Enzyme CAD: Its Function, Regulation, and Diagnostic Potential. Int. J. Mol. Sci. *22*, 10253. https://doi.org/10.3390/ijms221910253.
17. Del Caño-Ochoa, F., and Ramón-Maiques, S. (2021). Deciphering CAD: Structure and function of a mega-enzymatic pyrimidine factory in health and disease. Protein Sci. *30*, 1995–2008. https://doi.org/10.1002/pro.4158.
18. Shin, J., Mir, H., Khurram, M.A., Fujihara, K.M., Dynlacht, B.D., Cardozo, T.J., and Possemato, R. (2023). Allosteric regulation of CAD modulates de novo pyrimidine synthesis during the cell cycle. Nat. Metab. *5*, 277–293. https://doi.org/10.1038/s42255-023-00735-9.
19. Wang, T.Y., Zhao, J., Savas, A.C., Zhang, S., and Feng, P. (2020). Viral pseudoenzymes in infection and immunity. FEBS Journal *287*, 4300–4309. https://doi.org/10.1111/febs.15545.
20. Massière, F., and Badet-Denisot, M.A. (1998). The mechanism of glutamine-dependent amidotransferases. Cell. Mol. Life Sci. *54*, 205–222. https://doi.org/10.1007/s000180050145.
21. Cui, J., Yao, Q., Li, S., Ding, X., Lu, Q., Mao, H., Liu, L., Zheng, N., Chen, S., and Shao, F. (2010). Glutamine deamidation and dysfunction of ubiquitin/NEDD8 induced by a bacterial effector family. Science *329*, 1215–1218. https://doi.org/10.1126/science.1193844.
22. Sanada, T., Kim, M., Mimuro, H., Suzuki, M., Ogawa, M., Oyama, A., Ashida, H., Kobayashi, T., Koyama, T., Nagai, S., et al. (2012). The Shigella flexneri effector OspI deamidates UBC13 to dampen the inflammatory response. Nature *483*, 623–626. https://doi.org/10.1038/nature10894.
23. Flatau, G., Lemichez, E., Gauthier, M., Chardin, P., Paris, S., Fiorentini, C., and Boquet, P. (1997). Toxin-induced activation of the G protein p21 Rho by deamidation of glutamine. Nature *387*, 729–733. https://doi.org/10.1038/42743.
24. Schmidt, G., Sehr, P., Wilm, M., Selzer, J., Mann, M., and Aktories, K. (1997). Gln 63 of Rho is deamidated by Escherichia coli cytotoxic necrotizing factor-1. Nature *387*, 725–729. https://doi.org/10.1038/42735.
25. He, S., Zhao, J., Song, S., He, X., Minassian, A., Zhou, Y., Zhang, J., Brulois, K., Wang, Y., Cabo, J., et al. (2015). Viral pseudo-enzymes activate RIG-I via deamidation to evade cytokine production. Mol. Cell *58*, 134–146. https://doi.org/10.1016/j.molcel.2015.01.036.
26. Zhao, J., Zeng, Y., Xu, S., Chen, J., Shen, G., Yu, C., Knipe, D., Yuan, W., Peng, J., Xu, W., et al. (2016). A Viral Deamidase Targets the Helicase Domain of RIG-I to Block RNA-Induced Activation. Cell Host Microbe *20*, 770–784. https://doi.org/10.1016/j.chom.2016.10.011.
27. Zhao, J., Tian, M., Zhang, S., Delfarah, A., Gao, R., Rao, Y., Savas, A.C., Lu, A., Bubb, L., Lei, X., et al. (2020). Deamidation Shunts RelA from Mediating Inflammation to Aerobic Glycolysis. Cell Metab. *31*, 937–955.e7. https://doi.org/10.1016/j.cmet.2020.04.006.
28. Tian, Y., Feng, T., Zhang, J., Meng, Q., Zhan, W., Tang, M., Liu, C., Li, M., Tao, W., Shu, Y., et al. (2025). Histone H1 deamidation facilitates chromatin relaxation for DNA repair. Nature *641*, 779–787. https://doi.org/10.1038/s41586-025-08835-0.
29. Qi, Y., Tan, Z., Chen, H., Xiao, Z., Zhang, L., Wu, B., Liu, C., Gao, Y., Yang, X., Wu, L., et al. (2025). Pyrimidine synthase CAD deamidates and inactivates p53. Cell Res. *35*, 520–523. https://doi.org/10.1038/s41422-025-01112-9.
30. Qin, C., Rao, Y., Yuan, H., Wang, T.Y., Zhao, J., Espinosa, B., Liu, Y., Zhang, S., Savas, A.C., Liu, Q., et al. (2022). SARS-CoV-2 couples evasion of inflammatory response to activated nucleotide synthesis. Proc. Natl. Acad. Sci. USA. *119*, e2122897119. https://doi.org/10.1073/pnas.2122897119.
31. Reid, M.A., Allen, A.E., Liu, S., Liberti, M.V., Liu, P., Liu, X., Dai, Z., Gao, X., Wang, Q., Liu, Y., et al. (2018). Serine synthesis through PHGDH coordinates nucleotide levels by maintaining central carbon metabolism. Nat. Commun. *9*, 5442. https://doi.org/10.1038/s41467-018-07868-6.
32. Hu, G.S., Zheng, Z.Z., He, Y.H., Wang, D.C., and Liu, W. (2023). CPPA: A Web Tool for Exploring Proteomic and Phosphoproteomic Data in Cancer. J. Proteome Res. *22*, 368–373. https://doi.org/10.1021/acs.jproteome.2c00512.
33. Ariav, Y., Ch'ng, J.H., Christofk, H.R., Ron-Harel, N., and Erez, A. (2021). Targeting nucleotide metabolism as the nexus of viral infections, cancer, and the immune response. Sci. Adv. *7*, eabg6165. https://doi.org/10.1126/sciadv.abg6165.

34. Villa, E., Ali, E.S., Sahu, U., and Ben-Sahra, I. (2019). Cancer Cells Tune the Signaling Pathways to Empower de Novo Synthesis of Nucleotides. Cancers *11*, 688. https://doi.org/10.3390/cancers11050688.
35. Dasgupta, S., Rajapakshe, K., Zhu, B., Nikolai, B.C., Yi, P., Putluri, N., Choi, J.M., Jung, S.Y., Coarfa, C., Westbrook, T.F., et al. (2018). Metabolic enzyme PFKFB4 activates transcriptional coactivator SRC-3 to drive breast cancer. Nature *556*, 249–254. https://doi.org/10.1038/s41586-018-0018-1.
36. Meng, Y., Guo, D., Lin, L., Zhao, H., Xu, W., Luo, S., Jiang, X., Li, S., He, X., Zhu, R., et al. (2024). Glycolytic enzyme PFKL governs lipolysis by promoting lipid droplet-mitochondria tethering to enhance beta-oxidation and tumor cell proliferation. Nat. Metab. *6*, 1092–1107. https://doi.org/10.1038/s42255-024-01047-2.
37. Jiang, Y., Li, X., Yang, W., Hawke, D.H., Zheng, Y., Xia, Y., Aldape, K., Wei, C., Guo, F., Chen, Y., et al. (2014). PKM2 regulates chromosome segregation and mitosis progression of tumor cells. Mol. Cell *53*, 75–87. https://doi.org/10.1016/j.molcel.2013.11.001.
38. Guo, D., Tong, Y., Jiang, X., Meng, Y., Jiang, H., Du, L., Wu, Q., Li, S., Luo, S., Li, M., et al. (2022). Aerobic glycolysis promotes tumor immune evasion by hexokinase2-mediated phosphorylation of IκBα. Cell Metab. *34*, 1312–1324.e6. https://doi.org/10.1016/j.cmet.2022.08.002.
39. Moreno-Morcillo, M., Grande-García, A., Ruiz-Ramos, A., del Caño-Ochoa, F., Boskovic, J., and Ramón-Maiques, S. (2017). Structural Insight into the Core of CAD, the Multifunctional Protein Leading De Novo Pyrimidine Biosynthesis. Structure *25*, 912–923.e5. https://doi.org/10.1016/j.str.2017.04.012.
40. Lee, J.S., Adler, L., Karathia, H., Carmel, N., Rabinovich, S., Auslander, N., Keshet, R., Stettner, N., Silberman, A., Agemy, L., et al. (2018). Urea Cycle Dysregulation Generates Clinically Relevant Genomic and Biochemical Signatures. Cell *174*, 1559–1570.e22. https://doi.org/10.1016/j.cell.2018.07.019.
41. Wendler, P.A., Blanding, J.H., and Tremblay, G.C. (1983). Interaction between the urea cycle and the orotate pathway: studies with isolated hepatocytes. Arch. Biochem. Biophys. *224*, 36–48. https://doi.org/10.1016/0003-9861(83)90188-1.
42. Ge, T., Yang, J., Zhou, S., Wang, Y., Li, Y., and Tong, X. (2020). The Role of the Pentose Phosphate Pathway in Diabetes and Cancer. Front. Endocrinol. (Lausanne) *11*, 365. https://doi.org/10.3389/fendo.2020.00365.
43. Jiang, P., Du, W., and Wu, M. (2014). Regulation of the pentose phosphate pathway in cancer. Protein Cell *5*, 592–602. https://doi.org/10.1007/s13238-014-0082-8.
44. Song, J., Sun, H., Zhang, S., and Shan, C. (2022). The Multiple Roles of Glucose-6-Phosphate Dehydrogenase in Tumorigenesis and Cancer Chemoresistance. Life (Basel) *12*, 271. https://doi.org/10.3390/life12020271.
45. Wang, Y.P., Zhou, L.S., Zhao, Y.Z., Wang, S.W., Chen, L.L., Liu, L.X., Ling, Z.Q., Hu, F.J., Sun, Y.P., Zhang, J.Y., et al. (2014). Regulation of G6PD acetylation by SIRT2 and KAT9 modulates NADPH homeostasis and cell survival during oxidative stress. EMBO J. *33*, 1304–1320. https://doi.org/10.1002/embj.201387224.
46. Ma, X., Wang, L., Huang, D., Li, Y., Yang, D., Li, T., Li, F., Sun, L., Wei, H., He, K., et al. (2017). Polo-like kinase 1 coordinates biosynthesis during cell cycle progression by directly activating pentose phosphate pathway. Nat. Commun. *8*, 1506. https://doi.org/10.1038/s41467-017-01647-5.
47. Xu, H., Qing, X., Wang, Q., Li, C., and Lai, L. (2021). Dimerization of PHGDH via the catalytic unit is essential for its enzymatic function. J. Biol. Chem. *296*, 100572. https://doi.org/10.1016/j.jbc.2021.100572.
48. Wang, C., Wan, X., Yu, T., Huang, Z., Shen, C., Qi, Q., Xiang, S., Chen, X., Arbely, E., Ling, Z.Q., et al. (2020). Acetylation Stabilizes Phosphoglycerate Dehydrogenase by Disrupting the Interaction of E3 Ligase RNF5 to Promote Breast Tumorigenesis. Cell Rep. *32*, 108021. https://doi.org/10.1016/j.celrep.2020.108021.
49. Vandekeere, S., Dubois, C., Kalucka, J., Sullivan, M.R., García-Caballero, M., Goveia, J., Chen, R., Diehl, F.F., Bar-Lev, L., Souffreau, J., et al. (2018). Serine Synthesis via PHGDH Is Essential for Heme Production in Endothelial Cells. Cell Metab. *28*, 573–587.e13. https://doi.org/10.1016/j.cmet.2018.06.009.
50. Ma, C., Zheng, K., Jiang, K., Zhao, Q., Sha, N., Wang, W., Yan, M., Chen, T., Zhao, Y., and Jiang, Y. (2021). The alternative activity of nuclear PHGDH contributes to tumour growth under nutrient stress. Nat. Metab. *3*, 1357–1371. https://doi.org/10.1038/s42255-021-00456-x.
51. Yu, W., Wang, Z., Zhang, K., Chi, Z., Xu, T., Jiang, D., Chen, S., Li, W., Yang, X., Zhang, X., et al. (2019). One-Carbon Metabolism Supports S-Adenosylmethionine and Histone Methylation to Drive Inflammatory Macrophages. Mol. Cell *75*, 1147–1160.e5. https://doi.org/10.1016/j.molcel.2019.06.039.
52. Shen, L., Hu, P., Zhang, Y., Ji, Z., Shan, X., Ni, L., Ning, N., Wang, J., Tian, H., Shui, G., et al. (2021). Serine metabolism antagonizes antiviral innate immunity by preventing ATP6V0d2-mediated YAP lysosomal degradation. Cell Metab. *33*, 971–987.e6. https://doi.org/10.1016/j.cmet.2021.03.006.
53. Shu, Y., Hao, Y., Feng, J., Liu, H., Li, S.T., Feng, J., Jiang, Z., Ye, L., Zhou, Y., Sun, Y., et al. (2022). Non-canonical phosphoglycerate dehydrogenase activity promotes liver cancer growth via mitochondrial translation and respiratory metabolism. EMBO J. *41*, e111550. https://doi.org/10.15252/embj.2022111550.
54. Pacold, M.E., Brimacombe, K.R., Chan, S.H., Rohde, J.M., Lewis, C.A., Swier, L.J.Y.M., Possemato, R., Chen, W.W., Sullivan, L.B., Fiske, B.P., et al. (2016). A PHGDH inhibitor reveals coordination of serine synthesis and one-carbon unit fate. Nat. Chem. Biol. *12*, 452–458. https://doi.org/10.1038/nchembio.2070.
55. Possemato, R., Marks, K.M., Shaul, Y.D., Pacold, M.E., Kim, D., Birsoy, K., Sethumadhavan, S., Woo, H.K., Jang, H.G., Jha, A.K., et al. (2011). Functional genomics reveal that the serine synthesis pathway is essential in breast cancer. Nature *476*, 346–350. https://doi.org/10.1038/nature10350.
56. Mullarky, E., Lucki, N.C., Beheshti Zavareh, R., Anglin, J.L., Gomes, A.P., Nicolay, B.N., Wong, J.C.Y., Christen, S., Takahashi, H., Singh, P.K., et al. (2016). Identification of a small molecule inhibitor of 3-phosphoglycerate dehydrogenase to target serine biosynthesis in cancers. Proc. Natl. Acad. Sci. USA. *113*, 1778–1783. https://doi.org/10.1073/pnas.1521548113.
57. Wei, L., Lee, D., Law, C.T., Zhang, M.S., Shen, J., Chin, D.W.C., Zhang, A., Tsang, F.H.C., Wong, C.L.S., Ng, I.O.L., et al. (2019). Genome-wide CRISPR/Cas9 library screening identified PHGDH as a critical driver for Sorafenib resistance in HCC. Nat. Commun. *10*, 4681. https://doi.org/10.1038/s41467-019-12606-7.
58. Liang, C., Rieder, E., Hahm, B., Jang, S.K., Paul, A., and Wimmer, E. (2005). Replication of a novel subgenomic HCV genotype 1a replicon expressing a puromycin resistance gene in Huh-7 cells. Virology *333*, 41–53. https://doi.org/10.1016/j.virol.2004.12.031.
59. Yu, M., Bardia, A., Aceto, N., Bersani, F., Madden, M.W., Donaldson, M.C., Desai, R., Zhu, H., Comaills, V., Zheng, Z., et al. (2014). Cancer therapy. Ex vivo culture of circulating breast tumor cells for individualized testing of drug susceptibility. Science *345*, 216–220. https://doi.org/10.1126/science.1253533.
60. Iriondo, O., Liu, Y., Lee, G., Elhodaky, M., Jimenez, C., Li, L., Lang, J., Wang, P., and Yu, M. (2018). TAK1 mediates microenvironment-triggered autocrine signals and promotes triple-negative breast cancer lung metastasis. Nat. Commun. *9*, 1994. https://doi.org/10.1038/s41467-018-04460-w.
61. Li, S., Song, Y., Quach, C., Guo, H., Jang, G.B., Maazi, H., Zhao, S., Sands, N.A., Liu, Q., In, G.K., et al. (2019). Transcriptional regulation of autophagy-lysosomal function in BRAF-driven melanoma progression and chemoresistance. Nat. Commun. *10*, 1693. https://doi.org/10.1038/s41467-019-09634-8.

62. He, S., Zhao, Z., Yang, Y., O'Connell, D., Zhang, X., Oh, S., Ma, B., Lee, J.H., Zhang, T., Varghese, B., et al. (2015). Truncating mutation in the autophagy gene UVRAG confers oncogenic properties and chemosensitivity in colorectal cancers. Nat. Commun. *6*, 7839. https://doi.org/10.1038/ncomms8839.

63. Yang, C., Stueve, T.R., Yan, C., Rhie, S.K., Mullen, D.J., Luo, J., Zhou, B., Borok, Z., Marconett, C.N., and Offringa, I.A. (2018). Positional integration of lung adenocarcinoma susceptibility loci with primary human alveolar epithelial cell epigenomes. Epigenomics *10*, 1167–1187. https://doi.org/10.2217/epi-2018-0003.

64. Gregory, M.D., Ofosu-Asante, K., Lazarte, J.M.S., Puente, P.E., Tawfeeq, N., Belony, N., Huang, Y., Offringa, I.A., and Lamango, N.S. (2024). Treatment of a mutant KRAS lung cancer cell line with polyisoprenylated cysteinyl amide inhibitors activates the MAPK pathway, inhibits cell migration and induces apoptosis. PLoS One *19*, e0312563. https://doi.org/10.1371/journal.pone.0312563.

65. Yang, X.D., Tajkhorshid, E., and Chen, L.F. (2010). Functional interplay between acetylation and methylation of the RelA subunit of NF-kappaB. Mol. Cell. Biol. *30*, 2170–2180. https://doi.org/10.1128/mcb.01343-09.

66. Heinrich, P., Kohler, C., Ellmann, L., Kuerner, P., Spang, R., Oefner, P.J., and Dettmer, K. (2018). Correcting for natural isotope abundance and tracer impurity in MS-, MS/MS- and high-resolution-multiple-tracer-data from stable isotope labeling experiments with IsoCorrectoR. Sci. Rep. *8*, 17910. https://doi.org/10.1038/s41598-018-36293-4.

67. Chen, G., and Deng, X. (2018). Cell Synchronization by Double Thymidine Block. Bio Protoc. *8*, e2994. https://doi.org/10.21769/BioProtoc.2994.

68. Javanmoghadam-Kamrani, S., and Keyomarsi, K. (2008). Synchronization of the cell cycle using lovastatin. Cell Cycle (Georget. Tex.) *7*, 2434–2440. https://doi.org/10.4161/cc.6364.

STAR★METHODS

KEY RESOURCES TABLE

REAGENT or RESOURCE	SOURCE	IDENTIFIER
Antibodies		
Mouse monoclonal anti-CPS2 (CAD) (F-6)	Santa Cruz Biotechnology	Cat# sc-376072; RRID: AB_10989102
Rabbit polyclonal anti-CAD	Bethyl Laboratories	Cat# A301-374A-T; RRID: AB_937745
Mouse monoclonal anti-α-Tubulin (DM1A)	Cell Signaling Technology	Cat# 3873; RRID: AB_1904178
Mouse monoclonal anti-beta Actin (mAbcam 8226)	Abcam	Cat# ab8226; RRID: AB_306371
Mouse monoclonal anti-RELA/NFkB P65 (A-12)	Santa Cruz Biotechnology	Cat# sc-514451; RRID: AB_2891257
Mouse monoclonal anti-FLAG (M2)	Sigma-Aldrich	Cat# F3165; RRID: AB_259529
Rabbit monoclonal anti-G6PD (D5D2)	Cell Signaling Technology	Cat# 12263; RRID: AB_2797861
Rabbit monoclonal anti-PHGDH (D8F3O)	Cell Signaling Technology	Cat# 66350; RRID: AB_2737030
Rabbit polyclonal anti-V5	Bethyl Laboratories	Cat# A190-120A; RRID: AB_67586
Mouse monoclonal anti-GST (1E5)	Santa Cruz Biotechnology	Cat# sc-53909; RRID: AB_783586
Rabbit polyclonal anti-phospho-CAD (Ser1859)	Cell Signaling Technology	Cat# 12662; RRID: AB_2750934
Rabbit polyclonal anti-cyclin A	Santa Cruz Biotechnology	Cat# sc-751; RRID: AB_631329
Mouse monoclonal anti-cyclin B1 (V152)	Cell Signaling Technology	Cat# 4135; RRID: AB_2233956
Mouse monoclonal anti-cyclin E1 (HE12)	Cell Signaling Technology	Cat# 4129; RRID: AB_2071200
Biological samples		
HCC patient tumor and non-tumor tissues	This paper	N/A
Chemicals, peptides, and recombinant proteins		
Anti-FLAG M2 Affinity Gel	Sigma-Aldrich	Cat# A2220; RRID: AB_10063035
3X FLAG Peptide	Sigma-Aldrich	Cat# F4799
Anti-V5 Agarose Affinity Gel	Sigma-Aldrich	Cat# A7345; RRID: AB_10062721
Uridine	Sigma-Aldrich	Cat# U3003; CAS# 58-96-8
L-Dihydroorotic acid	Sigma-Aldrich	Cat# D7128; CAS# 5988-19-2
D-Glucose-6-phosphate (G6P) (sodium salt)	Cayman Chemical	Cat# 20376; CAS# 54010-71-8
NADP$^+$ (hydrate)	Cayman Chemical	Cat# 21045
NADPH	Cayman Chemical	Cat# 9000743; CAS# 2646-71-1
D-(−)-3-Phosphoglyceric Acid (sodium salt)	Cayman Chemical	Cat# 20123; CAS# 80731-10-8
NAD$^+$ (free acid)	Cayman Chemical	Cat# 16077; CAS# 53-84-9
NADH (sodium salt hydrate)	Cayman Chemical	Cat# 16078; CAS# 1949720-50-6
[U-^{13}C]Glucose	Cambridge Isotope Lab	Cat# CLM-1396; CAS# 110187-42-3
[1,2-^{13}C]Glucose	Cambridge Isotope Lab	Cat# CLM-504; CAS# 138079-87-5
Immobiline DryStrip pH 3-10NL, 7 cm	Cytiva	Cat# 17600112
Glutathione Sepharose 4B	Cytiva	Cat# 17075601
L-Glutathione reduced	Sigma-Aldrich	Cat# G6013; CAS# 70-18-8
G6PDi-1	MedChemExpress	Cat# HY-W107464; CAS# 2457232-14-1
NCT-503	MedChemExpress	Cat# HY-101966; CAS# 1916571-90-8-1
Thymidine	Sigma-Aldrich	Cat# T1895; CAS# 50-89-5
Lovastatin	LKT Labs	Cat# M1678; CAS# 75330-75-5
(±)-Mevalonolactone	Sigma-Aldrich	Cat# M4667; CAS# 674-26-0
Glutamine	Sigma-Aldrich	Cat# 1294808; CAS# 56-85-9
L-Glutamic acid	Sigma-Aldrich	Cat# G8415; CAS# 56-86-0

(*Continued on next page*)

Continued

REAGENT or RESOURCE	SOURCE	IDENTIFIER
Trypan Blue Solution	ThermoFisher	Cat# 15250061
DMEM (Dulbecco's Modified Eagle's Medium) Powder w/o glucose, glutamine & sodium pyruvate	CORNING	Cat# 90-113-PB
Dulbecco's MEM (DMEM) w/o Glucose, Glutamine, Serine, Glycine, Sodium Pyruvate (Powder)	USBiological Life Sciences	Cat# D9802-01
Sodium Pyruvate, Liquid 100 mM Solution	CORNING	Cat# 25-000-CI
Deposited data		
Metabolomics data	This paper	MetaboLights: MTBLS13498
Proteomics data for identifying CAD-binding proteins	This paper	PRIDE: PXD052153
Proteomics data for identifying deamidation sites of G6PD and PHGDH	This paper	PRIDE: PXD052165; PXD055217; PXD064420
Unprocessed gels and blots	This paper	Mendeley Data: 10.17632/85tsr8c2h8.1
Experimental models: Cell lines		
HepG2	ATCC	Cat# HB-8065
Huh7	Dr. Chengyu Liang, Wistar[58]	N/A
MCF7	Dr. Min Yu, UMD[59]	N/A
MDAMB231	Dr. Min Yu, UMD[60]	N/A
HCT116	ATCC	Cat# CCL-247
HT29	Dr. Chengyu Liang, Wistar[61]	N/A
LIM2045	Dr. Chengyu Liang, Wistar[62]	N/A
H522	Dr. Ite A. Offringa, USC[63]	N/A
H1648	Dr. Ite A. Offringa, USC[63]	N/A
H23	Dr. Ite A. Offringa, USC[64]	N/A
H358	Dr. Ite A. Offringa, USC[27]	N/A
A549	Dr. Ite A. Offringa, USC[63]	N/A
Rela-KO MEFs	Dr. Linfeng Chen, UIUC[65]	N/A
HEK293T	ATCC	Cat# CRL-3216
RKO	Dr. Chengyu Liang, Wistar[62]	N/A
SW480	Dr. Chengyu Liang, Wistar[62]	N/A
LoVo	Dr. Chengyu Liang, Wistar[62]	N/A
SW620	Dr. Chengyu Liang, Wistar[62]	N/A
RelA-KO MCF7	This paper	N/A
HepG2 G6PD Flag knockin	This paper	N/A
HepG2 PHGDH Flag knockin	This paper	N/A
LoVo G6PD Flag knockin	This paper	N/A
LoVo PHGDH Flag knockin	This paper	N/A
Experimental models: Organisms/strains		
NU/J mouse strain	Jackson Laboratory	Cat# 002019; RRID: IMSR_JAX:002019
Oligonucleotides		
Human CAD shRNA	ThermoFisher	N/A
Human UMPS shRNA	ThermoFisher	N/A
Other oligos for shRNAs or sgRNAs, see Table S1	This paper	N/A
Recombinant DNA		
CAD-pMXS-IRES-BLAST	Jong Shin et al.[18]	Addgene Plasmid # 188118
CAD-pcDNA5/FRT/TO	Jun Zhao et al.[27]	N/A

(*Continued on next page*)

Continued

REAGENT or RESOURCE	SOURCE	IDENTIFIER
GLN-pMXS-IRES-BLAST	This paper	N/A
GLN-pcDNA5/FRT/TO	This paper	N/A
G6PD-pCDH-CMV	This paper	N/A
G6PD-pGEX-4T-1	This paper	N/A
PHGDH-pCDH-CMV	This paper	N/A
PHGDH-pGEX-4T-1	This paper	N/A
Software and algorithms		
Graphpad Prism 9	Graphpad	http://www.graphpad.com
RStudio	Posit	https://posit.co/

EXPERIMENTAL MODEL AND STUDY PARTICIPANT DETAILS

Cells

HEK293T, Huh7, MDA-MB-231, HCT116, HT29, LIM2045, SW620, SW480, and *Rela*$^{-/-}$ mouse embryonic fibroblasts (MEF) were cultured in Dulbecco's modified Eagle's medium (DMEM, HyClone) supplemented with 10% heat-inactivated fetal bovine serum (FBS; Gibco), penicillin (100 U/ml), and streptomycin (100 mg/ml). HepG2, MCF7, and RKO were cultured in Eagle's Minimum Essential Medium (ATCC) supplemented with 10% FBS and antibiotics. H522, H1648, H23, and H358 cells were cultured in RPMI 1640 medium supplemented with 10% FBS and antibiotics. LoVo cells were cultured in F12K medium (Thermofisher) supplemented with 10% FBS and antibiotics.

Clinical samples

Subjects who underwent partial hepatectomy or liver transplant for hepatocellular carcinoma were included in this study, under an approved Institutional Review Board protocol (HS-15-00135, HS-15-00634, HS-17-00591). The cancerous tissue was retrieved from a section of liver tissue through gross examination, and a portion of the tissue was then subjected to histopathological confirmation. The adjacent non-cancerous liver tissue is at a minimum distance of 3 cm from the cancer tissue. The tissue samples were snap-frozen using liquid nitrogen and then stored at -80 °C until later analysis.

Mice

All animal work was performed under strict accordance with the recommendation in the Guide for the Care and Use of Laboratory Animals of the National Institutes of Health. The protocol was approved by the Institutional Animal Care and Use Committee (IACUC) of the University of Southern California (protocol number: 11730). Inbred and outbred female homozygous *Foxn1*^{nu} mice (6 weeks of age) were purchased from the Jackson Laboratory and were subjected to sterile animal housing. Mice (7-week-old) were used for all tumor xenograft experiments. Mice were randomized into different treatment and control groups equilibrated for body weight and age. Mice were fed with a regular sterile diet and maintained under specific pathogen-free conditions in an individually ventilated rack HEPA-filtered system on a 12:12 light cycle with average temperatures ranging from 70°F to 74°F. Direct bedding consists of either "Sani-Chips" (hardwood chips) or "Diamond Dry" paper processing by-product.

Plasmids

The human CAD and UMPS constructs were purchased from Thermo Scientific. Human CAD and mouse CAD sgRNAs were cloned into the pL-CRISPR.EFS.PAC-puro plasmid. sgRNAs of human RelA and CAD were cloned into the lentiCRISPR v2-hygro plasmid. Human G6PD and PHGDH sgRNAs for gene deletion or Flag knockin were cloned into the lentiCRISPR v2-blasticidin or lentiCRISPR v2-hygro plasmid, respectively. Human G6PD, PHGDH, and CAD shRNAs targeting their 3′UTR were cloned into the pLKO-hygro plasmid. Sequences of all oligos of sgRNAs and shRNAs are in Table S2. pMXS-IRES-BLAST-EGFP-Flag-CAD was purchased from Addgene (#188118). The GLN of CAD was cloned into pcDNA5/FRT/TO, pMXS-IRES-BLAST, and pCDH-CMV-EF1-Puro for transient and stable expression. Cancer-associated GLN mutations were generated by site-directed mutagenesis and confirmed by sequencing. Lentiviral expression constructs containing G6PD-WT, G6PD-N153D/Q161E, G6PD-N153A/Q161A, PHGDH-WT, PHGDH-Q439E/Q446E/N449D, and PHGDH-Q439A/Q446A/N449A were cloned into plasmids of pCDH-CMV-EF1-Puro, pCDH-CMV-EF1-Hygro, or pGEX-4T-1. The pcDNA5/FRT/TO-CAD-Flag, pcDNA5/FRT/TO-CAD-C252S-Flag, luciferase reporter plasmids for the NF-κB and RelA were described previously.[27]

METHOD DETAILS

Production of lentivirus or retrovirus

Lentiviral constructs (i.e., lentiCRISPR, pCDH, pGIPZ, pLKO) were transfected into 293T cells together with psPAX2 and pMD2.G for lentiviral production. Retroviral constructs (i.e., pMXS) were transfected into 293T cells together with the retroviral packaging vectors

Gag-Pol and CMV VSV-G for retroviral production. All transfections were done by calcium phosphate transfection. At 48 hours post transfection, the medium was collected and filtered through the 0.45 μm membrane. Retrovirus containing full-length CAD was concentrated by ultracentrifugation at 32,000 rpm for 2 hours (4°C). All viruses were aliquoted and frozen in -80°C.

Construction of gene knockdown, gene-deleted, Flag knockin, and reconstituted cell lines

Gene knockdown and gene-deleted cells were generated using shRNA and the CRISPR-CAS9 system, respectively. Lentivirus containing shRNA or sgRNA was added to cells for spin infection with 8 μg/ml polybrene at 1,800 rpm for 45 min. At 48 hours post-infection, antibiotics (i.e., 2 μg/ml puromycin, 200 μg/ml hygromycin, or 10 μg/ml blasticidin) were used to select cells. After selection, cells were ready to use or after single colony selection. Protein expression in cells with targeted gene knockdown or deletion was confirmed by immunoblotting.

To add a Flag epitope sequence to the endogenous G6PD or PHGDH, HepG2 or LoVo cells were seeded into a 10-cm dish to achieve 70% confluency and were transfected with lentiCRISPR v2-hygro plasmids containing a target sequence complementary to the intron that locates upstream of the ATG of G6PD or PHGDH plus a donor plasmid containing homologous arms and the Puro-P2A-3×Flag sequence. After 48 h, the medium containing 2 μg/ml puromycin was added to select for tagged cells. After selection, the cells were diluted and seeded into a 96-well plate at 0.5 cell/well in complete media. Wells that contained a single colony were expanded until enough cells were available for total protein extraction and determining Flag-G6PD or Flag-PHGDH via immunoblotting.

To establish reconstituted cell lines, cells were infected with hygromycin-resistant lentiviral shRNA targeting the 3′UTR of G6PD, PHGDH, or CAD or blasticidin-resistant lentiviral sgRNA targeting G6PD or PHGDH. Depletion of G6PD, PHGDH, or CAD was validated by immunoblotting. G6PD- or PHGDH-depleted cells were infected with puromycin-resistant lentivirus containing wild-type, deamidated or deamidation-resistant mutants of G6PD or PHGDH. CAD-depleted cells were infected with blasticidin-resistant retrovirus containing wild-type CAD, CAD-S44F, CAD-F335S, or CAD-E347Q. G6PD- and PHGDH-deleted cells were infected with hygromycin-resistant lentivirus containing wild-type, deamidated or deamidation-resistant mutants of G6PD, and puromycin-resistant lentivirus containing wild-type, deamidated or deamidation-resistant mutants of PHGDH. Reconstituted cells were then selected and maintained with corresponding antibiotics and protein expression was validated by immunoblotting.

Cell proliferation assay

Cells were counted and plated in triplicate in 12-well or 6-well plates, with initial seeding density of 20,000 cells (12-well plates) or 40,000 cells (6-well plates) per well. Viable cells were counted with trypan blue solution at indicated time points.

Carboxyfluorescein succinimidyl ester (CFSE) staining

Cells were gently suspended in pre-warmed (37°C) PBS containing CFSE working solution at the appropriate concentration (1 μM). Incubate the cells for 20 minutes at 37°C to label the cells. Pellet the labeled cells by centrifugation and resuspend in fresh pre-warmed culture medium. After three days, cells were digested, stained with propidium iodide (PI) solutions, and read by flow cytometry. CFSE intensity in alive cells was analyzed.

Xenograft nude mouse model

To determine the effects of CAD depletion or G6PD/PHGDH deamidation on tumor growth, a total of 5×10^6 cells in 100 μl mixture of PBS and Matrigel (Corning) were injected subcutaneously in the dorsal flank of the mice (n = 4). Tumor size was measured with calipers every three days. The tumor volume was calculated using the equation: Volume = $(\text{length} \times \text{width}^2)/2$. Tumors were harvested and weighed when mice were euthanized.

To determine the sensitivity of cells with high or low deamidation to G6PD and PHGDH inhibitors, a total of 5×10^6 HT29, RKO, or LIM2045 cells in 100 μl mixture of PBS and Matrigel (Corning) were injected subcutaneously in the dorsal flank of the mice (n = 8). When tumors became established (minimum 100 mm^3), the animals were randomized and divided into two groups. One group received intraperitoneal G6PDi-1 (MedChemExpress, # HY-W107464) plus NCT-503 (MedChemExpress, # HY-101966) (10 mg/kg body weight in 5% DMSO, 95% corn oil, every two days) and the other group was injected with the vehicle. Tumor sizes were measured with calipers every three days. Tumors were harvested and weighed when mice were euthanized.

Two-dimensional gel electrophoresis

Cells were lysed in rehydration buffer (7 M Urea, 2 M Thiourea, 2% CHAPS, 0.5% IPG Buffer, 0.002% bromophenol blue) by two pulses of sonication and whole cell lysates were centrifuged at 13k rpm for 15 min. Supernatants were loaded to IEF strips (pH 3-10NL, 7 cm, Cytiva, #17600112) for focusing with a program comprising of: 20 V, 10 h (rehydration); 500 V, 1 h; 1000 V, 1 h; 1000-5000 V, 4 h; 5000 V, 5 h. After IEF, strips were incubated with SDS equilibration buffer (50 mM Tris-HCl [pH8.8], 6 M urea, 30% glycerol, 2% SDS, 0.001% Bromophenol Blue) containing 10 mg/ml DTT for 15 min and then SDS equilibration buffer containing 2-iodoacetamide (25 mg/ml) for 15 min. Strips were washed with SDS-PAGE buffer, resolved by SDS-PAGE, and analyzed by immunoblotting.

Metabolite profiling and isotope tracing

Metabolite pool size analysis was done by using 2×10^6 cells per sample. Cells were washed on ice with 1 ml ice-cold 150 mM ammonium acetate (NH_4AcO, pH 7.3), and 1 ml of -80°C cold 80% MeOH was added to the wells. Samples were incubated at -80°C for 30 min, and cells were scraped off and supernatant was transferred into microfuge tubes. Samples were pelleted at 4°C for 10 min at 15k rpm. The supernatant was transferred into new microfuge tubes. Metabolites were dried at room temperature under vacuum. For isotope tracing experiments, cells were washed with PBS and cultured with tracing medium for indicated hours before metabolite extraction. Cells reconstituted with G6PD-WT, G6PD-DE, or G6PD-AA were traced with DMEM (w/o glucose and glutamine) (CORNING, #90-113-PB) supplemented with 10% dialyzed FBS (Gibco), 2 mg/ml [U-^{13}C]Glucose (Cambridge Isotope Lab, # CLM-1396), or [1,2-^{13}C]Glucose (Cambridge Isotope Lab, # CLM-504) and 4 mM glutamine. PHGDH-depleted cells reconstituted with PHGDH-WT, PHGDH-EED, or PHGDH-AAA or GLN-expressing cells were traced with DMEM (w/o Glucose, Glutamine, Serine, Glycine) (USBiological Life Sciences, # D9802-01) supplemented with 10% dialyzed FBS (Gibco), 2 mg/ml [U-^{13}C]Glucose and 4 mM glutamine. To determine isotope labelling of metabolites in the PPP such as 6PG and R5P, cells were traced with [U-^{13}C]glucose or [1,2-^{13}C]glucose for 5 min. Additional tracing using [U-^{13}C]glucose, cells were labeled for: i) 30 min to determine metabolites of the SSP (i.e., 3PS, serine); ii) 4 h to determine m+5 fraction of purine or pyrimidines; iii) 10 h to determine m+2 glycine, m+6-9 purines, m+6-9 SAM, or m+6-8 pyrimidines.

Snap-frozen paired tumor and tumor-adjacent biopsies from HCC patients were weighed and balanced to 25 mg per sample. Tissue samples were further cut into small pieces, kept on dry ice, and homogenized in 1 ml of 80% methanol using Zirconia/Silica Beads by beats beater (Bio Spec Products Inc.). Homogenized tissues were incubated with methanol in -80°C for 30 min. Extracts were separated from cell debris by centrifuging at 15,000 rpm at 4°C for 10 min. The pellet was re-extracted with another 0.2 ml cold 80% methanol and the supernatant was added to the first extract. Metabolites were dried under vacuum. The remaining cellular pellet was resuspended in 100 μl protein lysis buffer and the protein concentration was determined. Equivalent amounts of extracts were used for the LC-MS run.

Dried metabolites were re-suspended in water for the LC-MS run. Briefly, samples were randomized and analyzed on a Q-Exactive Plus hybrid quadrupole-Orbitrap mass spectrometer coupled to Vanquish UHPLC system (Thermo Fisher). The mass spectrometer was run in polarity switching mode (+3.00 kV/-2.25 kV) with an m/z window ranging from 65 to 975. Mobile phase A was 5 mM NH_4AcO, pH 9.9, and mobile phase B was acetonitrile. Metabolites were separated on a Luna 3 μm NH2 100 NH2 100Å (150 x 2.0 mm) column (Phenomenex). The flow rate was 0.3 ml/min, and the gradient was from 15% A to 95% A in 18 min, followed by an isocratic step for 9 min and re-equilibration for 7 min. All samples were run in biological replicates. Metabolites were detected and quantified as the area under the curve based on retention time and accurate mass using the TraceFinder 4.1 (Thermo Scientific) software. Metabolite pool size analysis was performed using both cell number and median normalization. Raw abundance data are available in Table S2. Tracing data was corrected for natural isotope abundance and tracer impurity using the IsoCorrectoR package.[66]

Protein expression and purification

Flag-CAD, Flag-GLN, Flag-G6PD, and Flag-PHGDH were purified from transfected HEK293T cells or Flag-knockin cells. Cells were harvested and lysed with Triton X-100 buffer (20 mM Tris, pH 7.5, 150 mM NaCl, 1.5 mM MgCl2, 20 mM β-glycerophosphate, 1 mM sodium orthovanadate, 10% glycerol, 0.5 mM EGTA, 0.5% Triton X-100) supplemented with a protease inhibitor cocktail (Roche). Whole cell lysates were sonicated and centrifuged at 12,000 rpm for 15 min. The supernatant was collected, filtered, pre-cleared with protein A/G agarose beads at 4°C for 1 h and then incubated with anti-Flag M2 agarose (Sigma-Aldrich, #A2220) at 4°C for 4 h. The agarose beads were washed extensively and eluted with 0.2 mg/ml 3xFlag peptide (Sigma-Aldrich, # F4799). The eluted proteins were analyzed by SDS gel electrophoresis and Coomassie brilliant blue (CBB) staining.

GST-G6PD and GST-PHGDH were purified from bacteria. Briefly, *E. coli* BL21 (*DE3*) was induced with 1 mM IPTG at 16°C for 12 h. Cells were harvested by centrifugation and lysed with Triton X-100 buffer (20 mM Tris, pH 7.5, 150 mM NaCl, 1.5 mM MgCl2, 10% glycerol, 0.5 mM EGTA, 1% Triton X-100). After sonication and centrifugation, cell lysates were incubated with glutathione Sepharose 4B beads (GE Healthcare) for 4 h at 4°C. Sepharose beads were washed extensively, eluted by 10 mM reduced glutathione (if necessary), and analyzed by CBB staining.

Co-immunoprecipitation (co-IP) and immunoblotting

Whole cell lysates were prepared with NP40 buffer (50 mM Tris-HCl, pH 7.4, 150 mM NaCl, 1% NP-40, 5 mM EDTA) supplemented with 20 mM β-glycerophosphate, 1 mM sodium orthovanadate, and a protease inhibitor cocktail (Roche). Whole cell lysates were sonicated and centrifuged. The supernatant was pre-cleared with protein A/G agarose for 1 h. Pre-cleared samples were incubated with indicated protein A/G agarose conjugated with antibodies for 4 h at 4°C. The agarose beads were washed extensively, and samples were eluted by boiling at 95°C for 10 min. Precipitated proteins were analyzed by SDS gel electrophoresis followed by immunoblotting.

All immunoblotting was performed using the indicated primary antibodies. Proteins were visualized by the Odyssey infrared imaging system (LI-COR) followed by incubation with IRDye800-conjugated secondary antibodies (1:10,000 dilution, LI-COR). In some experiments (e.g., Figures 3L, 3M, and 4N), the same membrane was sequentially probed with indicated antibodies and visualized using different channels of secondary antibodies.

Crosslinking assay

DSS crosslinking was used to detect the G6PD and PHGDH oligomers. Briefly, cells were digested with trypsin and counted. Equal number of cells (1x10 ˆ6 cells) were collected for experiment. Cells were washed with PBS and resuspended in conjugation buffer (20 mM HEPES, pH = 8.0). The DSS solution prepared in DMSO was added to the cell suspension to a final concentration of 1 mM. After incubating at 37 °C for 30 min, the samples were boiled and used for protein detection by western blot assays.

In vitro deamidation assay

In an Eppendorf tube, 0.2 μg of CAD or GLN, and 0.4 μg of GST-G6PD or GST-PHGDH (bound to glutathione-conjugated agarose) were added to a total volume of 30 μl. The reaction was carried out at 30°C for 45 min in the deamidation buffer (100 mM Tris–HCl at pH 8.0, 100 mM KCl, 1 mM dithiothreitol, 20.2 mM aspartate, 1.5 mM ATP, 200 mM phosphoribosyl 5′-pyrophosphate, 3.5 mM $MgCl_2$, and 5 mM $NaHCO_3$). After reaction, protein-loaded glutathione agarose was washed briefly with 0.1 M sucrose solution. GST-G6PD or GST-PHGDH was eluted with the rehydration buffer (7 M Urea, 2 M Thiourea, 2% CHAPS, 0.5% IPG Buffer, 0.002% bromophenol blue) at room temperature. Samples were then analyzed by two-dimensional gel electrophoresis and immunoblotting.

For in vitro deamidation followed by LC-MS/MS analysis, peptide or protein substrates were used. For peptides, 5 μg of bead-conjugated CAD or the glutaminase inactive mutant CAD-C252S (CS) purified from 293T cells was incubated with the G6PD peptide containing deamidation residues for 45 minutes. Deamidated peptides in the supernatant were purified using C18 columns and quantified by LC-MS. For proteins, G6PD/PHDGH and CAD were purified from bacteria and 293T cells, respectively. G6PD/PHGDH (loaded to glutathione beads) was incubated with or without CAD for 45 mins and subjected to mass spectrometry analysis after on-beads or in-gel digestion.

Size exclusion chromatography

Purified proteins were loaded to Superose 6 column and subjected to gel filtration analysis with PBS. Elution was collected in 0.8 ml per fraction, and proteins in each fraction were precipitated with trichloroacetic acid (TCA) and analyzed by western blot after resuspended in loading buffer. Bovine serum albumin, alcohol dehydrogenase from yeast, and β-Amylase from sweet potato were run as size markers.

Cell cycle synchronization

(1) S phase synchronization: HepG2 cells were seeded at 25% confluency and then synchronized by double thymidine block method as previously described.[67] Briefly, cells were cultured in their corresponding medium containing 2 mM thymidine (Sigma-Aldrich, # T1895) for 18 h then replaced with fresh medium for 9 h, followed by a second thymidine block (2 mM) for 18 h to synchronize cells at the G1/S boundary. Upon release by replacing the medium with a fresh one, cells were harvested at multiple time points for western blotting, two-dimensional gel electrophoresis, or protein purification. (2) G0/G1 phase synchronization: MCF7 cells were seeded at 40% confluency and then synchronized by lovastatin method.[68] Briefly, cells were arrested in G0/G1 phase by incubation with the medium containing lovastatin (LKT Labs, # M1678) (10 μM) for 36 h. Upon release by replacing the medium with that containing 1 mM mevalonate (Sigma-Aldrich, #M4667), cells were harvested at multiple time points for western blotting and two-dimensional gel electrophoresis.

Glutaminase assay

Roughly 100 ng CAD or CAD mutant proteins purified from transiently transfected 293T cells were incubated with glutamine (ranging from 20 mM to 156 μM) in reaction buffer (100 mM Tris-HCl at pH 8.0, 100 mM KCl, 1 mM dithiothreitol) at 30 °C for 45 min. The concentration of produced glutamate was determined by LC-MS with a parallel running of glutamate stand.

Dual-luciferase reporter assay

HEK293T cells were transfected with NF-κB reporter plasmid cocktail (50 ng of luciferase reporter plasmid and 5 ng of pRL Renilla luciferase control vector) and expression plasmid (empty plasmid or pcDNA5/FRT/TO-GLN) by calcium phosphate precipitation. Whole cell lysates were used to determine the activity of firefly luciferase and Renilla luciferase by a microplate reader (FLUOstar Omega) at 24 h post transfection.

G6PD and PHGDH enzymatic assay

Purified wild-type and mutant proteins of G6PD or PHGDH were determined by CBB staining. Protein concentration was quantified using the BCA Protein Assay Kit (Thermo Scientific, #23225).

Approximately 20 ng of G6PD or mutant proteins were added to 100 μl G6PD enzymatic assay buffer (50 mM triethanolamine hydrochloride and 5 mM EDTA, pH 7.5) containing 0.5 mM $NADP^+$. After incubating for 5 min, 0.66 mM G6P was added to the reaction and absorbance was quantified under 340 nm of the plate reader in a time-series plate mode. To determine enzyme kinetics, reactions containing constant G6P (1 mM) and increasing concentration of $NADP^+$ (4 μM to 4 mM), or constant $NADP^+$ (2 mM) and increasing concentration of G6P (10 μM to 1.5 mM) were carried out. In addition, an NADPH standard curve in G6PD enzymatic assay buffer was added to quantify NADPH production.

Approximately 1 μg PHGDH was used to measure its enzymatic activity. PSAT1 and its substrate glutamate were included to prevent the inhibition of PHGDH by its product. The PHGDH assay buffer consists of 50 mM HEPES, PH 7.5, 1 mM EDTA, 2 mM 3PG, 2 mM NAD^+, 30 mM glutamate, 80 ng/μl PSAT1. Absorbance was quantified under 340 nm of the plate reader in a time-series plate mode. To determine the enzyme kinetics, reactions containing constant 3PG (4 mM) and increasing concentration of NAD^+ (125 μM to 16 mM) or constant NAD^+ (8 mM) and increasing concentrations of 3PG (125 μM to 8 mM) were carried out. In addition, an NADH standard curve in PHGDH assay buffer was added to quantify NADH production.

Proteomics

To identify CAD-binding proteins, CAD and its binding proteins were precipitated with Anti-Flag M2 agarose beads from HepG2 cells stably expressing Flag-CAD. After washing five times with 20 mM ammonium bicarbonate (pH:7.8), 10 mM DTT in 100 mM ammonium bicarbonate (pH:7.8) was added to the beads for reduction in a 37°C shaker for 30 min. Then, alkylation was performed by adding an equal volume of 25 mM IAA to the DTT bead suspension and rotating in the dark for 30 min at room temperature. Proteins were then digested by trypsin (1:100 enzyme/substrate ratio, 37°C shaker, overnight). Peptides were desalted with C18 Toptip and then dried in a rotary evaporator. To identify deamidation sites, G6PD or PHGDH was purified from transfected 293T cells or FLAG knockin HepG2 cells and subject to SDS gel electrophoresis and CBB staining. Protein bands were excised for in-gel digestion. G6PD was digested by trypsin and PHGDH was digested sequentially with trypsin and chymotrypsin due to the absence of lysine and arginine at the C terminal.

Purified peptides were re-suspended in 0.1% formic acid for LC-MS run. Briefly, peptides separated with the C18 Acclaim PepMap column (75 μm id × 15 cm, 2 μm particle sizes,100 Å pore sizes, Thermo Scientific) were ionized at 1.9 kV in the positive ion mode. MS1 survey scans were acquired at the resolution of 70,000 from 350 to 1800 m/z, with a maximum injection time of 100 ms and AGC target of 1e6. MS/MS fragmentation of the 14 most abundant ions were analyzed at a resolution of 17,500, AGC target 5e4, maximum injection time 65 ms, and normalized collision energy of 26. Dynamic exclusion was set to 20 s and ions with a charge of +1, +7 and >+7 was excluded. MS/MS fragmentation spectra were searched with Proteome Discoverer SEQUEST (version 2.4, Thermo Scientific) against the in silico tryptic digested Uniprot all-reviewed Homo sapiens database (release June 2017, 42,140 entries). The maximum missed cleavages were set to 3. Dynamic modifications were set to oxidation on methionine (M, +15.995 Da) and deamidation on asparagine and glutamine (N and Q, +0.984 Da). Carbamidomethylation on cysteine residues (C, +57.021 Da) was set as a fixed modification. The maximum parental mass error was set to 10 ppm, and the MS/MS mass tolerance was set to 0.03 Da. The false discovery threshold was set strictly to 0.01 using the Percolator Node validated by q-value. The relative abundance of parental peptides was calculated by integration of the area under the curve of the MS1 peaks using the Minora LFQ node. Spectral annotation was generated by the Interactive Peptide Spectral Annotator (IPSA, http://www.interactivepeptidespectralannotator.com/).

Data mining

Data on the relative protein abundance and phosphorylation levels in cancer and adjacent tissues were retrieved from the National Cancer Institute's Clinical Proteomic Tumor Analysis Consortium (CPTAC) and the National Cancer Institute's International Cancer Proteogenome Consortium (ICPC) datasets using Cancer Proteogenomic Data Analysis Site (cProSite) web-based tool, URL: https://cprosite.ccr.cancer.gov/ (accessed on 20 January 2023). CAD was set as a target protein. CAD hazard ratio and survival estimate curve for liver cancer patients were collected from Cancer Proteome and Phosphoproteome Atlas (CPPA) (https://cppa.site/cppa).[32] Hazard ratio was analyzed by setting LIHC as tumor type, overall survival, Tertiles as cutoff, high expression with pool prognosis. The Kaplan–Meier (KM) model is used to calculate the survival probability along with death event and survival time. Tertiles was set as stratification methods to classify samples into either high or low expression groups according to CAD protein abundance. All CAD mutations were analyzed from TumorPortal (http://www.tumorportal.org/) based on The Cancer Genomic Atlas (TCGA) database. CAD was set as the targeted gene and all cancer types were analyzed similarly.

QUANTIFICATION AND STATISTICAL ANALYSIS

Statistical analysis was performed using GraphPad Prism software for the two-way ANOVA test, one-way ANOVA test, or paired/unpaired two-tailed Student's *t*-test. p values of < 0.05 were considered statistically significant for each test.